Precambrian Research 364 (2021) 106361

Contents lists available at ScienceDirect

Precambrian Research

journal homepage: www.elsevier.com/locate/precamres

Oxidizing atmosphere and life on land during the late Paleoproterozoic outset of the "boring billion"

Gregory J. Retallack [a,*], Zhong-Qiang Chen [b], Yuangan Huang [b], Yuheng Fang [b]

[a] Department of Earth Sciences, University of Oregon, Eugene, OR 97403, USA
[b] State Key Laboratory of Biogeology and Environmental Geology, School of Earth Science, China University of Geosciences (Wuhan), Wuhan 430078, China

ARTICLE INFO

Keywords:
Mesoproterozoic
Paleosol
North China
Atmospheric oxygen
Carbon dioxide

ABSTRACT

The so called "boring billion" (1800–800 Ma) of Late Paleoproterozoic and early Mesoproterozoic time can now be reassessed from the evidence of diverse paleosols in the Ruyang Group (1749–1561 Ma) in Henan Province, China. Widespread marine sulfidic facies is the reason for the term "boring billion", but terrestrial facies and paleosols were far from uniform or anoxic at that time. The Ruyang Group in Henan has 12 distinct kinds of paleosols, with 5 distinct pedotypes in alluvial fan facies of the Bingmagou Formation, 6 in fluvial facies of the Yunmengshan Formation, 3 in coastal plain facies of the Baicaoping Formation, and 4 in the coastal to intertidal Beidajian Formation. These paleosols are evidence of hyperarid climate that was cool temperate despite proximity to the paleoequator. These ancient soils were alive with iron- and manganese-fixing bacteria that created desert varnish and vesicular structure, as well as sulfur-oxidizing bacteria creating desert roses of gypsum. The paleosols may also have supported cyanobacteria, algae and fungi, known from palynomorphs in shales of the Baicaoping and Beidajian formations. Consumption of alkali and alkaline earth elements in the paleosols are evidence of 1700–20,600 ppm (6–73 times preindustrial level or PAL) of atmospheric CO_2, consistent with the amount needed for a greenhouse effect to offset a faint young sun. A comparable model based on iron and manganese oxidation in the paleosols indicates 318–16,623 ppm (0.002–0.08 PAL) O_2. This was enough to support animals (0.005 PAL O_2), considering that these are minimal estimates of O_2 diluted by some soil respiration. Animals had not yet evolved, but that evolutionary process may not have been limited by atmospheric composition.

1. Introduction

The interval between 1800 and 800 Ma has been known as the "boring billion" of Earth history, because it lacks major events in marine rocks, which include a lot of pyritic dysaerobic shales (Buick et al., 1995). The Statherian period (1800–1600 Ma) of the late Paleoproterozoic extending through the Mesoproterozoic (1600–1000 Ma) is seen as a "long period of stable one-celled-life ecosystems in apparently constant environments" (Ogg et al. 2016). However, it was a time of remarkable evolutionary diversification of acritarchs, including multicellular red algae and fungi (Agić et al., 2017; Mukherjee et al., 2018). The 1750–1600 Ma Ruyang Group of Henan Province, North China has been especially productive of such microfossils (Yin, 1997; Yin et al., 2004; Yin et al., 2005; Li et al., 2012; Li et al., 2020) and putative "trace fossils" (Yang and Zhou 1995; Huang et al., 2010; Tang et al., 2011; Zheng et al., 2012), and has been interpreted as a shallow marine and alluvial sequence on the southern margin of the North China Craton (Hu et al., 2014; Yue et al., 2018). This study of paleosols formed at the outset of the boring billion aims to reconstruct life on land and atmospheric composition at that time.

Paleosols, or soils of the past exposed to the atmosphere for millennia, have long been important guides to atmospheric composition (Serdyuchenko, 1968). The chemical and mineral composition of their parent materials is substantially altered by millennia of exposure to atmospheric oxygen, which oxidizes and fixes iron and manganese, and to carbon dioxide, which as carbonic acid displaces alkali and alkaline earth elements (Holland, 1984). These effects have been modeled to provide estimates of atmospheric O_2 and CO_2 from net losses and gains of elements within paleosols (Sheldon, 2006; Retallack, 2018), and these techniques are here applied to the Statherian Ruyang Group of central China. Was the boring billion a time of low atmospheric oxidation and high carbon dioxide greenhouse as inferred from marine records? And what, if any, role was played by life on land during the Mesoproterozoic diversification of life on Earth?

* Corresponding author.

https://doi.org/10.1016/j.precamres.2021.106361
Received 30 December 2020; Received in revised form 6 August 2021; Accepted 10 August 2021

2. Geological background

The Ruyang Group crops out in hill ranges to the north and west of floodplains of the Huang He ("Yellow River"), in northern and western Henan Province, North China (Fig. 1). It is a sequence of sandstone, with red beds (Fig. 2), gray shales and some stromatolitic dolostones, deposited on the southern margin of the North China Craton (Hu et al., 2014), in alluvial fan, fluvial, and shallow marine paleoenvironments (Zheng et al., 2008; Zheng et al., 2011; Zheng et al., 2016). This area was within and flanking an intracratonic rift of the Xiong'er Group basalts during the initial breakup of the Nuna supercontinent at low paleolatitudes (Zhang et al., 2012). The basal unit of the Ruyang Group is the Bingmagou Formation, cropping out near Luoyang City at the Wananshan section (Fig. 1 and Fig. 4A), where it overlies Archean schists of the Dengfeng Group, and is succeeded by the Yunmengshan, Baicaoping and Beidajian formations (Su et al., 2012; Zheng et al., 2017; Yue et al., 2018). Further north near Jiaozou City in Yuntaishan Geopark, Yunmengshan Formation overlies Archean (3399–2511 Ma) gneiss and trondhjemite of the Dengfeng Group, and is overlain by Cambrian sandstones (Gao et al., 2006; Zheng et al., 2008; Zheng et al., 2011). To the south near Lushan in the Wanghuazhuang section (Fig. 4B), Xiong'er Group basalts are overlain by the Yunmengshan, Baicaoping and Beidajian formations (Zheng et al., 2012). A 2-m-thick basalt flow at 80 m in the Wanghuazhuang section (Fig. 1 and Fig. 4B) is evidence of continuation of Xiong'er Group rift basaltic volcanism.

Basalts of the Xiong'er Group have been radiometrically dated at 1750–1800 Ma (Zhao et al., 2002; Zhao et al., 2004; Yue et al., 2018). A weighted mean U/Pb detrital zircon approximation of depositional age for the lowest Yunmengshan Formation is 1744 ± 22 Ma (Hu et al., 2014). A U-Pb age of 1611 ± 8 Ma comes from a tuff within stromatolitic dolostones of the Luoyukou Formation of the Luoyu Group, overlying the Ruyang Group (Su et al., 2012). In the Sanjiaotang Formation of the Luoyu Group diagenetic xenotime cements have been dated at 1411 ± 27 Ma (Lan et al., 2014). A similar age of detrital zircons of 1743 ± 72 Ma from the lower Beidajian Formation (Li et al., 2020), is essentially recycled from the Yunmengshan Formation. The three useful ages in the composite section of Wanan (Fig. 1 and Fig. 4A) and Wanghuazhuang sections (Fig. 4) yield a model for age (M) from stratigraphic level (L), with $r^2 = 0.99$, standard error ± 18 Ma, and F-test p = 0.001

$$M = -0.0718L + 1799.3 \quad (1)$$

This age model predicts a total age range for the Ruyang Group of 1749–1561 Ma.

3. Materials and methods

Detailed stratigraphic sections were prepared near Ludian at Wananshan starting at N34.50028° E112.62179° (Fig. 4) and near Lushan at Wanghuazhuang village starting at N33.78979° E112.63475° (Fig. 5). Oriented rock samples were collected of suspected paleosols for laboratory studies, including bulk chemical composition (Table 1). Additional observations were made in Hongshi Gorge of Yuntaishan Geopark near Jaiozhou (N35.42798° E113.35699°). Thin sections were used to quantify grain size (Table 2) and mineral compositions (Table 3) by point counting (500 points) using a Swift automated stage and Hacker counting box on a Leitz Orthoplan Pol research microscope. These 500-point counts have accuracy ±2% for common constituents (Murphy, 1983). Major and trace element chemical analysis was determined by XRF in fused beads at China University of Sciences, Wuhan (R5532-5564, 5582-5624), and by ALS Chemex in Vancouver (R5567-5579), Canada. Bulk density was measured by the clod method: from raw weight, then clods coated in paraffin of known density, in and out of chilled (6°C) water (Retallack, 2019b).

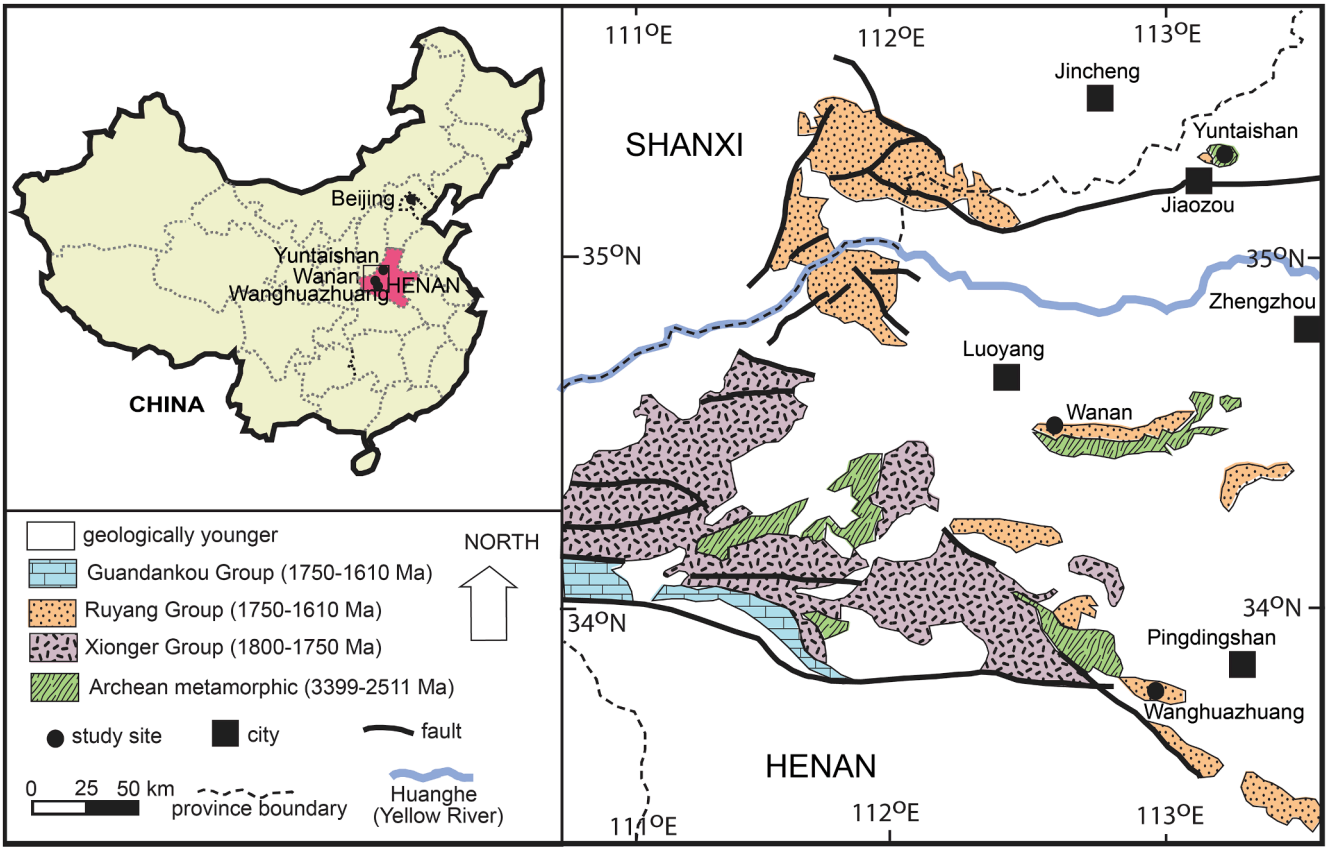

Fig. 1. Map of visited localities of the Ruyang Group, in Henan Province, China (after Yue et al., 2018).

Fig. 2. Alluvial sedimentary facies: A, Hougou paleosols with desert roses 100 m below local top of Yunmengshan Formation in Hongshi Gorge, near Yuntaishan (N35.43063° E113.35828°); B, oversize clasts of quartzite and conglomerate in sandstone 45 m above base of Yunmengshan Formation in Wanghuazhuang section (N35.7902° E112.65275°); C, Xiaoshan pedotype (at hammer) over Jeipan at 280 m in Bingmagou Formation near Wananshan (N34.50402° E112.62238°); D, Alluvial ripple marks with wind scours and microbial mat drapes in upper Yunmengshan Formation near Yuntaishan (N35.42949° E113.35825°); E, Mudcracks in red claystone of Lushan pedotype filled with sandstone in upper Yunmengshan Formation near Yuntaishan (N35.41754° E113.37174°).

4. Metamorphic and diagenetic alteration

Paleosols represent early diagenetic alteration during the interval between deposition and burial, which must be disentangled from late diagenesis and metamorphism before paleoenvironmental interpretation. The Ruyang Group demonstrates three early diagenetic alterations common in red beds (Retallack 1991a): (1) drab mottles in upper portions of beds due to burial gleization of buried organic matter, (2) dark red (Munsell 10R) color from dehydration reddening of ferric hydroxide minerals, and (3) substantial lithostatic compaction. Burial gleization is chemical reduction of oxides and hydroxides of iron by anaerobic bacteria on subsidence into anoxic water, and is especially suggested by drab mottles and tubular features radiating down from bed tops (Fig. 3A, C), as in Cambrian (Álvaro et al., 2003; Retallack, 2008) and Proterozoic red beds (Driese et al., 1995; Retallack, 2013). Such geologically ancient red beds are also brick red in color from burial dehydration of ferric oxyhydroxides (Fig. 3A–C), unlike brown to yellow modern soils and late Pleistocene sediments (Retallack 1991a).

The Ruyang group is flat-lying to gently dipping (Fig. 2A,C). With highly variable potash values of 0.25 to 5.89 wt% (Table 1), there is little evidence of pervasive potash metasomatism (Novoselov and de Souza Filho, 2015). Burial compaction (C as %) can be calculated as 73 ± 3 % from ptygmatic deformation of clastic dikes in the Dawaling paleosol (45 m in Fig. 4B) and 76 ± 3 % from ptygmatically folded clastic dikes in the Wanghua paleosol (1025 m in Fig. 4B). Burial compaction (C as %) can also be calculated from the 2.8 km of Paleozoic overburden to the Luoyu Group (Zuo et al., 2019) for each level in the composite Wananshan-Wanghuazhuang section using Eq. (2), based on total depth of burial (B in km) and physical constants for Aridisols of 0.51, 0.49, and 0.27 (Sheldon and Retallack 2001).

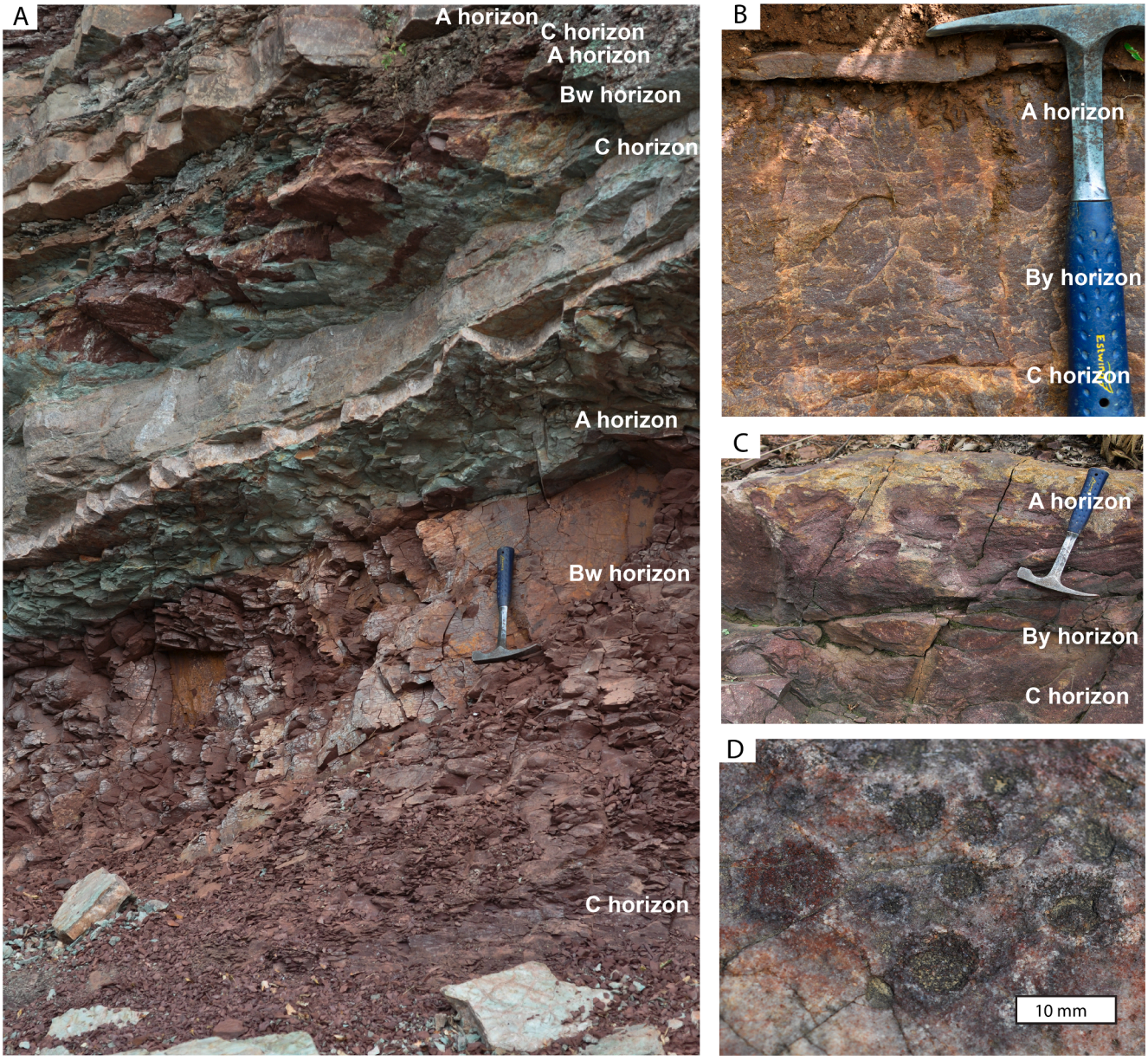

Fig. 3. Mesoproterozoic paleosols: A, succession of drab topped red paleosols, from top Lushan, Jeipan and Wanghua pedotypes at 1025 m in Baicaoping Formation near Wanghuazhuang village (N33.78102° E112.66504°); B, Hougou pedotype in upper Yunmengshan Formation near Yuntaishan (N33.42798° E112.35699°); C, Dawaling pedotype at 511 m in Yunmengshan Formation in Wanghuazhuang section (N33.79479° E112.63729°): D, desert roses after gypsum in Hougou pedotype 530 m in Yunmengshan Formation in Wanghuazhuang section (N33.79016° E112.65279°).

$$C = \frac{-0.51 \times 100}{\left\{\left(\frac{\frac{0.49}{D}}{e^{0.27}}\right) - 1\right\}} \quad (2)$$

Calculated compaction was 70% for the top of the section and 75% at the base. Such compaction estimates are needed for paleoenvironmental interpretations based on original bed thicknesses (Retallack, 2005). Extensive compaction and silicification of sandstones and siltstones of the Ruyang Group, and oxidized clasts within drab beds (Fig. 7F), preclude significant Phanerozoic oxidative weathering of these rocks.

5. Paleosol recognition

Paleosols are definitively recognized in the field as horizons of fossil root traces (Retallack, 1977; Retallack, 1991b), but there were no rooted vascular land plants before Silurian (Retallack, 2015a). Without root traces, a variety of other features can be used to recognize paleosols in Precambrian non-marine facies. Field recognition of Precambrian paleosols relies on a variety of features such as soil cracking structures, pseudomorphs of sand crystals, nodules, and gradational color changes (Retallack, 2016). The following paragraphs consider these various paleosol criteria in turn.

5.1. Angular silt

Some thin sections show an even mix of sand, silt and clay grains, but others show overwhelmingly abundant, angular, silt size grains, particularly the base of the Wanghua profile in the Baicaoping Formation (Fig. 5), and Jeipan and Lushan profiles in the Bingmagou Formation (Fig. 6). These are not claystones as they appear in hand specimen, but grain-supported angular siltstone, and both are probably eolian deposits. The Wanghua siltstone is largely quartz and feldspar, like other parts of the Ruyang Group, but the Jiepan-Lushan example has

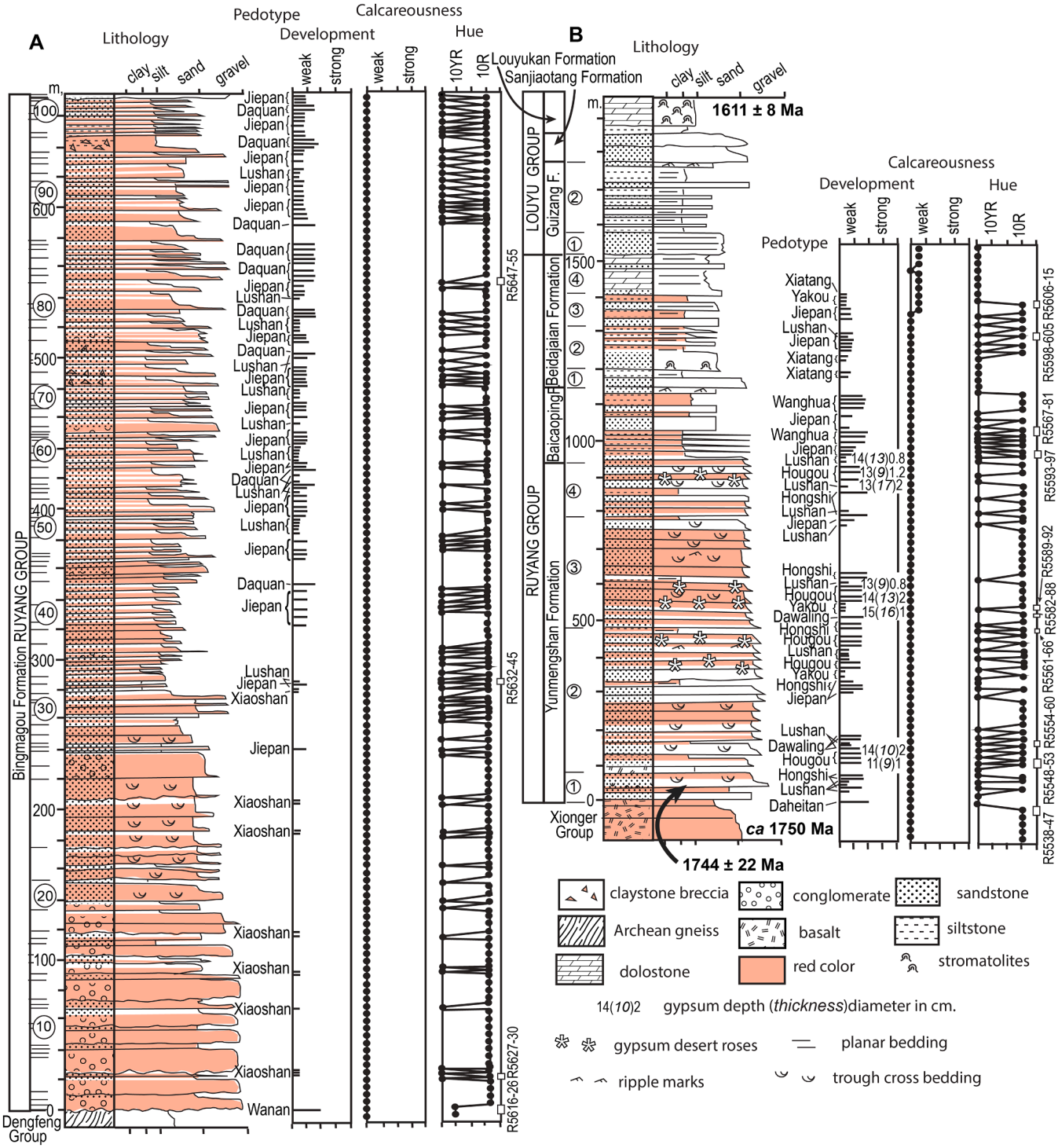

Fig.4. Measured sections of paleosols near Wananshan (A) and Wanghuazhuang (B), after Yue et al. (2018) and Tang et al. (2011), respectively.

unusually high amounts of biotite, and may be an airfall tuff. These loess deposits can be compared with late Quaternary Peoria Silt, which is volcaniclastic in Kansas and Nebraska (Swineford and Frye, 1951) but quartzose in Illinois and Mississippi (Pye and Sherwin, 1999, Bettis et al., 2003). These differences reflect proximity to Cordilleran volcanoes in Kansas and Nebraska, but proximity to deglaciated Archean granite and Paleozoic sediments from Wisconsin to Illinois. More eolian silt may have fallen into the sea before the advent of land plants, but silt grains are supported by clay and carbonate in Cambrian marine rocks (Dalrymple et al., 1985), rather than grain-supported and overwhelmingly silt, like two notable examples from the Ruyang Group (Figs. 5 and 6), which lack fine lamination or varves of marine or lacustrine shales.

5.2. *Wind-dissected ripples*

Straight crested and linguoid ripple marks of the Yunmengshan Formation were created by alluvial to shallow-marine traction currents, including symmetrical oscillation ripples and some bimodal current directions (Zheng et al., 2008). Highly asymmetric ripples with climbing

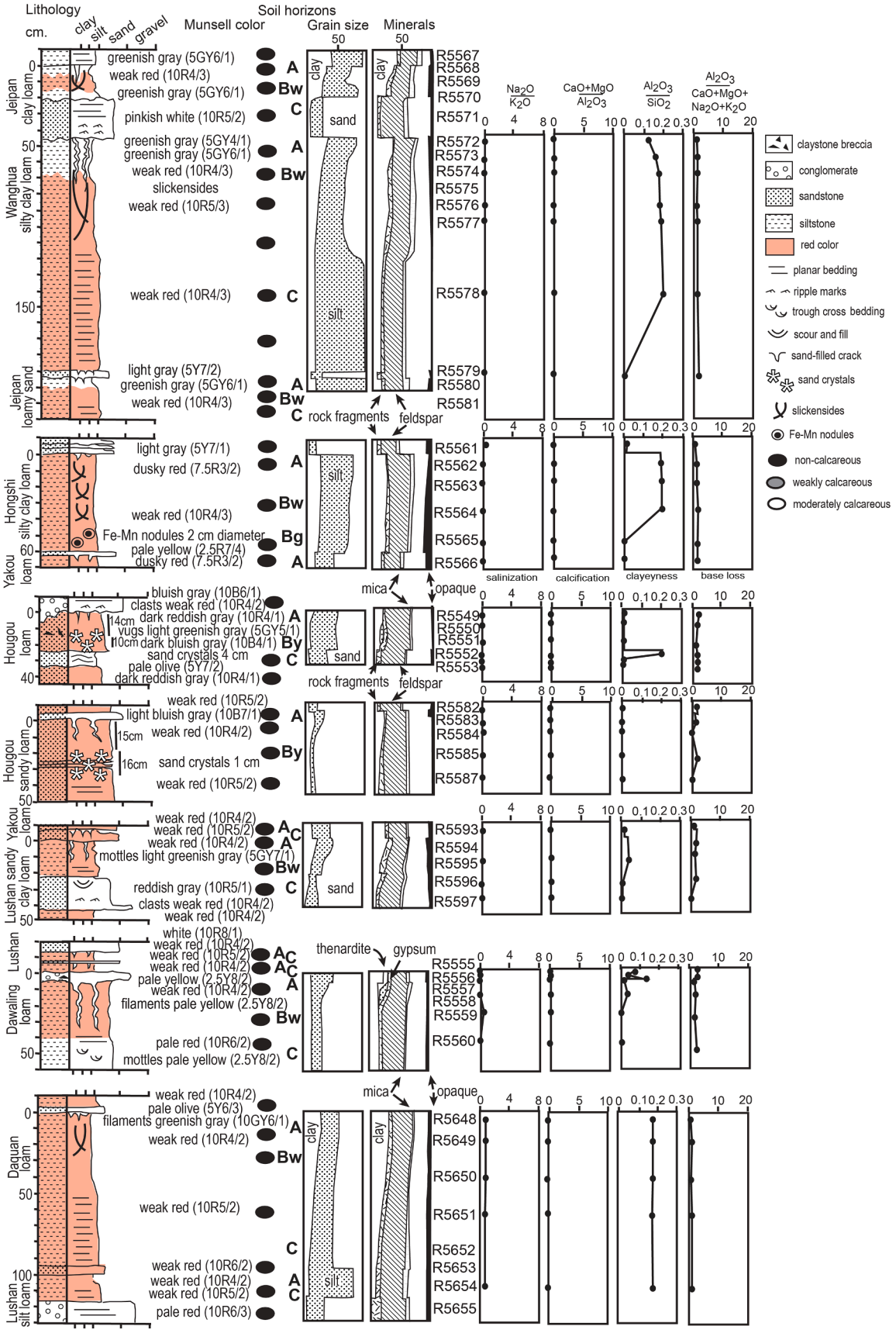

Fig.5. Petrographic and chemical composition of moderately developed paleosols.

Table 1
Chemical composition (wt %) from XRF of samples from Henan, China.

Pedotype.	Sample-	SiO_2	TiO_2	Al_2O_3	Fe_2O_3T	MnO	CaO	MgO	Na_2O	K_2O	P_2O_5	LOI	TOTAL	$g.cm^{-3}$
Daheitan	R5538	94.04	0.17	1.8	2.55	0.01	0.11	0.03	0.01	0.56	0.02	0.58	99.88	2.5740
Daheitan	R5539	87.3	0.43	5.68	2.92	0.01	0.4	0.23	0.01	1.97	0.16	1.27	100.38	2.5740
Daheitan	R5540	63.28	1.27	15.04	11.02	0.01	0.89	0.37	0.01	4.9	0.24	3.29	100.32	2.5913
Daheitan	R5541	65.89	1.35	16.28	6.6	0.01	0.85	0.48	0.01	5.19	0.34	3.42	100.42	2.6801
Daheitan	R5542	65.8	1.36	16.2	6.48	0.01	0.84	0.47	0.01	5.19	0.34	3.68	100.38	2.6801
Daheitan	R5543	58.98	1.44	17.11	10.94	0.02	1.35	0.41	0.01	5.59	0.27	4.29	100.41	2.6106
Hougou	R5549	95.11	0.09	1.83	1.31	0.01	0.09	0.01	0.01	0.73	0.01	0.44	99.64	2.5313
Hougou	R5550	95.41	0.08	1.78	1.26	0.01	0.11	0.01	0.04	0.67	0.01	0.56	99.94	2.5313
Hougou	R5551	95.95	0.06	1.29	1.02	0.01	0.07	0.02	0.04	0.52	0.01	1.32	100.31	2.1243
Hougou	R5552	96.87	0.07	1.17	0.49	0.01	0.04	0.01	0.01	0.48	0.01	0.47	99.63	2.4634
Hougou	R5553	95.63	0.09	2.09	0.34	0.01	0.1	0.02	0.01	0.83	0.02	0.53	99.67	2.5121
Lushan	R5554	77.99	0.45	9.84	5.12	0.01	0.63	0.08	0.01	3.06	0.05	2.87	100.11	2.6668
Lushan	R5554	78.6	0.45	9.8	4.99	0.01	0.63	0.07	0.01	3.05	0.05	2.73	100.39	2.6668
Lushan	R5555	68.5	0.7	14.62	7.06	0.01	0.92	0.12	0.01	4.53	0.04	3.88	100.39	2.5658
Dawaling	R5556	89.08	0.24	4.69	3.23	0.01	0.28	0.02	0.01	1.52	0.01	0.55	99.64	2.9187
Dawaling	R5557	95.12	0.08	2.08	0.87	0.01	0.13	0.05	0.01	0.65	0.01	0.67	99.68	2.9187
Dawaling	R5558	89.05	0.23	4.67	3.19	0.01	0.28	0.02	0.05	1.51	0.02	0.63	99.66	2.5833
Dawaling	R5559	97.57	0.06	0.75	0.67	0.01	0.06	0.01	0.07	0.24	0.01	0.25	99.7	2.5833
Dawaling	R5560	97.98	0.06	0.56	0.5	0.01	0.03	0.01	0.01	0.17	0.01	0.31	99.65	2.5763
Hongshi	R5561	92.79	0.16	2.02	2.92	0.01	0.13	0.02	0.3	0.79	0.02	0.56	99.72	2.6553
Hongshi	R5562	57.81	1.09	17.99	10.26	0.01	1.68	0.15	0.08	5.92	0.11	5.29	100.39	2.6553
Hongshi	R5563	55.74	1.08	17.75	10.48	0.02	1.86	0.19	0.08	6.04	0.152	5.76	99.21	2.6553
Hongshi	R5564	56.68	1.11	18.26	11.54	0.01	1.73	0.14	0.01	6.01	0.08	4.8	100.37	2.6705
Hongshi	R5564	56.6	1.11	18.12	11.31	0.01	1.72	0.17	0.01	6	0.08	5.28	100.41	2.6705
Hongshi	R5565	94.33	0.8	2.22	2.26	0.02	0.14	0.01	0.03	0.69	0.02	0.21	100	2.3471
Hongshi	R5566	92.72	0.1	2.13	4.1	0.03	0.14	0.02	0.03	0.66	0.022	−0.22	99.73	2.3471
Wanghua	R5573	67.41	0.55	14.62	3.61	0.02	1.71	0.38	0.1	6.28	0.21	4.01	99	2.6071
Wanghua	R5574	57.47	0.58	15.45	11.92	0.03	1.89	0.36	0.1	6.72	0.199	4.47	99.27	2.7636
Wanghua	R5575	56.41	0.7	17.18	10.05	0.06	2.21	0.41	0.1	7.29	0.226	4.86	99.58	2.8707
Wanghua	R5576	55.83	0.73	17.66	9.41	0.05	2.26	0.43	0.11	7.39	0.235	5.19	99.38	2.7883
Wanghua	R5578	53.58	0.68	18.06	11.12	0.04	2.24	0.46	0.11	7.27	0.252	5.39	99.26	2.7208
Wanghua	R5579	95.8	0.07	1.96	0.23	0.01	0.14	0.07	0.01	1.02	0.03	0.56	99.9	2.6602
Hougou	R5582	96.87	0.04	0.95	0.96	0.01	0.07	0.02	0.04	0.28	0.01	0.36	99.61	2.6676
Hougou	R5583	97.32	0.04	0.7	1.03	0.01	0.04	0.01	0.01	0.22	0.01	0.25	99.64	2.6338
Hougou	R5586	97.88	0.04	0.35	0.98	0.01	0.02	0	0.01	0.11	0.01	0.25	99.66	2.6910
Yakou	R5589	93.26	0.18	2.36	2.57	0.01	0.21	0.05	0.01	0.85	0.04	0.12	99.66	2.6668
Yakou	R5590	94.76	0.07	2.5	0.32	0.01	0.18	0.02	0.01	1.12	0.01	0.64	99.64	2.6668
Yakou	R5591	91.22	0.19	3.18	2.88	0.01	0.28	0.06	0.01	1.21	0.03	0.79	99.86	2.6668
Yakou	R5592	93.2	0.13	2.35	2.01	0.01	0.17	0.05	0.05	1.06	0.02	0.62	99.67	2.6668
Lushan	R5593	91.07	0.09	3.5	2.46	0.01	0.31	0.07	0.01	1.29	0.05	0.97	99.83	2.6668
Lushan	R5594	85.76	0.23	6.47	2.72	0.01	0.54	0.08	0.01	2.47	0.06	1.56	99.91	2.6668
Lushan	R5595	85.76	0.22	6.43	2.66	0.01	0.54	0.09	0.01	2.45	0.06	1.78	100.01	2.5658
Lushan	R5596	93.93	0.01	2.13	0.81	0.01	0.2	0.11	0.02	0.82	0.07	0.97	99.08	2.6170
Lushan	R5597	96.87	0.01	0.7	0.46	0.01	0.05	0.15	0.01	0.28	0.11	0.41	99.06	2.6511
Jeipan	R5599	52.04	0.81	22.53	6.3	0.01	3.12	0.37	0.02	8.47	0.15	6.58	100.4	2.6668
Jeipan	R5601	48.62	0.74	21.26	11.82	0.01	3.04	0.36	0.04	7.84	0.14	6.35	100.22	2.6308
Jeipan	R5602	95.24	0.04	2.25	0.4	0.01	0.26	0.14	0.01	0.82	0.1	0.81	100.08	2.5806
Lushan	R5603	53.2	0.72	20.34	9.23	0.01	2.93	0.42	0.02	7.78	0.17	5.58	100.4	2.6492
Lushan	R5604	53.69	0.71	20.63	9.42	0.01	2.94	0.41	0.02	7.82	0.17	4.51	100.33	2.5488
Lushan	R5605	88.61	0.11	2.8	5.03	0.01	0.36	0.54	0.01	1.06	0.37	1.51	100.41	2.8144
Xiatang	R5606	97.63	0.04	0.61	0.44	0.01	0.06	0.17	0.01	0.24	0.12	0.28	99.61	2.5872
Xiatang	R5607	98.01	0.04	0.77	0.24	0.01	0.03	0.01	0.01	0.42	0.01	0.26	99.81	2.5872
Xiatang	R5607	97.76	0.04	0.75	0.23	0.01	0.03	0.01	0.01	0.41	0.01	1.12	100.38	2.5872
Xiatang	R5608	99.02	0.04	0.44	0.22	0.01	0.02	0.01	0.01	0.19	0.01	0.21	100.18	2.6339
Yakou	R5609	97.81	0.05	0.8	0.27	0.01	0.05	0.04	0.01	0.32	0.01	0.33	99.7	2.5872
Yakou	R5610	98.27	0.04	0.63	0.21	0.01	0	0.03	0.01	0.13	0.01	0.36	99.7	2.6429
Yakou	R5611	98.39	0.03	0.53	0.2	0.01	0.01	0.02	0.01	0.24	0.01	0.22	99.67	2.6451
Yakou	R5612	97.68	0.03	0.85	0.27	0.01	0.02	0.01	0.01	0.5	0.01	0.27	99.66	2.6452
Yakou	R5613	97.95	0.03	0.67	0.43	0.01	0.02	0.02	0.01	0.29	0.01	0.18	99.62	2.6098
Yakou	R5614	95.48	0.05	2.13	0.34	0.01	0.06	0.02	0.01	1.41	0.01	0.3	99.82	2.5763
Yakou	R5615	96.61	0.06	1.25	0.47	0.01	0.16	0.09	0.01	0.47	0.05	0.43	99.61	2.6127
Wanan	R5616	62.24	1.69	13.85	6.58	0.16	2.31	2.35	3.1	2.78	0.73	4.58	100.37	1.9456
Wanan	R5617	57.55	1.3	15.83	7.61	0.14	3.4	1.75	2.79	2.14	0.33	7.56	100.4	1.9456
Wanan	R5617	57.36	1.3	15.72	7.46	0.14	3.44	1.77	2.8	2.09	0.32	7.57	99.97	1.9456
Wanan	R5618	45.93	0.8	15.49	11.78	0.38	7.68	3.63	1.34	0.51	0.07	12.79	100.4	1.9456
Wanan	R5619	43.36	0.99	15.49	12.93	0.28	7.97	3.91	0.82	0.39	0.1	13.47	99.71	1.9456
Wanan	R5620	46.9	1.01	15.58	10.94	0.26	9.23	5.53	1.14	0.61	0.09	8.31	99.6	1.9456
Wanan	R5621	49.56	0.98	14	13.73	0.2	6.92	9.16	1.41	0.53	0.07	3.84	100.4	2.2849
Wanan	R5622	46.4	0.58	14.13	9.74	0.17	4.43	12.96	1.33	1.81	0.04	8.06	99.65	2.7903
Wanan	R5623	50.07	0.73	12.67	11.51	0.19	6.49	9.21	2.38	0.77	0.08	5.48	99.58	2.8327
Wanan	R5624	59.15	0.84	14.75	7.59	0.15	3.92	6.45	3.76	0.77	0.21	2	99.59	2.7021
Wanan	R5624	58.98	0.82	14.77	7.54	0.15	3.88	6.42	3.76	0.78	0.21	2.29	99.6	2.7021
Daquan	R5648	58.72	0.94	17.45	7.33	0.06	2.58	0.64	2.43	4.21	0.261	4.58	99.26	2.5886
Daquan	R5649	57.62	0.93	17.54	7.99	0.06	2.71	0.59	2.37	4.34	0.225	4.54	98.98	2.5886
Daquan	R5650	57.62	0.97	17.42	7.8	0.06	2.7	0.71	2.49	3.93	0.283	4.77	98.81	2.5638
Daquan	R5651	56.61	1.01	17.86	8.57	0.05	2.92	0.71	2.25	4.2	0.261	5.1	99.61	2.5638

Errors are from 10 replicate analyses of the standard, CANMET SDMS2 (British Columbia granodioritic sand).

translatent stratification created by wind (Retallack and Mao 2019) were not seen, but some of the waterlain ripples show modifications after formation. Pervasive slight offsets are from burial jointing and veining, but scalloping orthogonal to ripple crests are best explained by wind scour (Fig. 2D), as also illustrated for the Yunmengshan Formation by Zheng et al. (2008) and Tang et al. (2011).

5.3. Rock avalanches

A scatter of cobbles was seen at 45 m in the Yunmengshan Formation (Fig. 4B) on the east side of the dam 100 m north of Daheitan village (N33.79844 E112.634794), and is striking in the separation of large angular to rounded cobbles within medium sandstone. The cobbles are a mix of quartzite, basalt, and fully lithified, roundstone, red, conglomerate on a single bedding plane (Fig. 2B). The sandstone above has numerous angular, pale red (10R6/3), clast-supported, claystone intraclasts, which are also found at the base of the 3 m sandstone supporting the scattered boulders. Another matrix-supported conglomerate with clasts up to 5 cm in diameter caps the Dawaling profile (Fig. 5 and Fig. 7A F) at 162 m in the Yunmengshan Formation in a road cut 350 m south of Daheitan (N33.79479° E112.63729°).

In both cases there is hydrodynamic incongruence between the size of the clasts and their matrix, unlike waterlain deposits of alluvial fans (Elmore, 1984), channel lags (Mader, 1985), or shingle beaches (Retallack, 1983). Nor is there associated frost-heave or ice wedge deformation of periglacial soils, described by Van Vliet-Lanoë (1998). Similar cobble-train, outsize-clast and clustered-clast conglomerates elsewhere have been attributed to cohesionless debris flows, with larger clasts falling and rolling from steep (5-17°) terrains (Kim et al., 1995; Sohn et al., 1999). The large clasts may thus be outriders of rock avalanches, also known as sturzstroms (Yarnold, 1993). The enclosing trough-cross-bedded sandstone with clast-supported red-intraclast breccias are not unusual, and have been widely reported in fluvial sandstones from collapse of floodplain cut banks and erosion of desiccation-cracked claystones (McBride, 1974; Retallack, 2019a).

5.4. Vesicular structure

Below the capping pebbly sandstone of the Dawaling profile discussed in the last section, thin sections reveal millimetric rounded vesicles. The original hollow nature of these is revealed by needles with the orthorhombic form and other mineral properties of thenardite (Na_2SO_4) radiating into the cavity (Fig. 7B). The cavity is now filled by opaque iron-manganese.

Vesicles form in igneous rocks like pumice and basalt, from degassing of flows released from original confining pressure (Aubele et al., 1988), but this Dawaling profile is a non-volcanic sandstone forming atop a fluvial paleochannel. Vesicular structure is a characteristic feature of the surface horizons of desert soils (McFadden et al., 1998), and thenardite is a common ephemeral salt effloresence in desert soils (Gibson et al., 1983; Hamdi-Aissa et al., 2004; Voigt et al., 2020). Two theories for the origin of vesicular soil structure is formation after a local downpour of rain, when dormant microbial communities produce gases that bubble up through muddy sediment (McFadden et al., 1998), or when saturated lower parts of the profile displace soil air upward (Lebedeva et al., 2019). Filling of the vesicles with iron-manganese may also reflect transient awakening of iron- and manganese-oxidizing bacteria following downpours (Lebedeva et al., 2019), which also cemented the uppermost part of the Dawaling profile below the clast-supported capping sandstone (Fig. 7F).

5.5. Rock varnish

Opaque cement of amorphous iron and manganese oxides are found near the surface of several beds, including Yakou (Fig. 7C), Hougou (Fig. 7D), and Dawaling (Fig. 7F) profiles. A thin rind of opaque cement most intense at the top is at the surface of the beds, but there also are coatings of claystone clasts near the surface (Fig. 7C), and pockets of stain with concentric structure, like ministromatolites laterally linked by connecting threads of opaque cement (Fig. 7D).

Desert varnish is a coating of colloidal iron and manganese oxides coating soils and rocks in deserts (Allen, 1978). Comparable encrustations also occur in lakes and rivers (Dorn and Oberlander, 1982) and as placic horizons in gleyed parts of soils (Wu and Chen, 2005), but in those cases are thicker and more continuous, lacking the discontinuous to ministromatolitic form of surface-soil and rock varnish (Krinsley et al., 1995; Garvie et al., 2008). The opaque oxides are formed by diverse communities, including iron- and manganese-oxidizing bacteria, which come alive from dormancy during rare rains (Taylor-George et al., 1983; Palmer et al., 1986). These examples as old as 1.6 Ga in the Yunmengshan Formation are not the oldest known examples of rock varnish in paleosols: rock varnish has also been noted in a 2.2 Ga paleosol (Retallack et al., 2013).

5.6. Crack patterns

Polygonal systems of cracks with v-shaped profile filled with sand in clay (Weinberger, 2001) are widespread in the Ruyang Group (Fig. 2E, Fig. 3C; Yang and Zhou, 1995; Zheng and Sun, 2011; Tang et al., 2011; Zheng et al., 2016; Yue et al., 2018). In other cases, the cracks are narrow, deep, and ptygmatically folded by burial compaction of the surrounding clayey matrix (Fig. 3A C). Neither of these deep contorted cracks are in especially clayey matrix: one (Fig. 3A, Fig. 5) is in siltstone, and the other (Fig. 3C, Fig. 6) is in sandstone. The enigma of sand cracking like clay has been explained by Prave (2002) as due to abundant hydrated microbiota, like that of a microbial earth soil (Retallack, 2012a). Alternative explanations may be frost cracking in a periglacial soil (Kokelj et al., 2007, Raffi and Stenni, 2011), but ice wedges are more strongly tapering than the Ruyang Group examples (Fig. 2A,C).

Soils have more complex cracks that simple desiccation polygons, with a network of intersecting modified surfaces known as cutans defining characteristic clod shapes, known as peds (Retallack, 2019b). Sesquans (iron and aluminum-stained cutans) defining blocky angular peds are ptygmatically folded by compaction below the laminated cover to paleosols (Fig. 3A-B). Microfabric of highly birefringent sheared clay in intersecting sets also is seen in the Baicaoping Formation (Fig. 7A), a diagnostic soil fabric reflecting the highly deviatoric stress fields induced by soil formation, and called clinobimasepic (Retallack, 2019b). These crack systems ranging on scales of meters to microns in size disrupt primary sedimentary structures to create the characteristic massive field appearance of paleosols (Fig. 3A–C). Marine or lacustrine sandstones and shales in contrast have clear lamination or varves (Zillen et al., 2003; Retallack and Jahren, 2008).

5.7. Sand crystals

Hougou profiles of the Yunmengshan Formation (Fig. 4B) have spherical to ellipsoidal spherulites of acicular sand crystals after gypsum ($CaSO_4{\cdot}2H_2O$) which form an horizon 9–16 cm think some 11–15 cm below the top of the profile (Fig. 3D, Fig. 5). The profile on a rock platform north of the Taoist shrine 1 km west of Wanghuazhuang village (N33.79016° E112.65279°) exposes many of these on a former bedding plane, and the diameters of 500 of them are shown in Fig. 8. Radiating laths of dark crystals are clear in the field (Fig. 3D), but more subtle in

Table 2
Grain-size data from point counting thin sections (500 points) of Ruyang Group.

Pedotype	Hoz	No.	% gravel	% sand	% silt	% clay	Textural class	Grain fabric	Plasmic fabric
Daheitan	above	R5539	0	43.6	32.8	23.6	loam	granular	silasepic
Daheitan	A	R5540	0	69.8	22.0	8.2	sandy loam	intertextic	crystic
Daheitan	A	R5541	0	70.0	28.2	1.8	sandy loam	intertextic	crystic
Daheitan	Bw	R5543	0	67.6	31.0	1.4	sandy loam	intertextic	crystic
Hougou	A	R5549	0	43.0	41.6	15.4	loam	intertextic	silasepic
Hougou	By	R5550	0	59.2	32.8	8.0	sandy loam	intertextic	silasepic
Hougou	By	R5551	0	56.6	33.4	10.0	sandy loam	granular	silasepic
Hougou	C	R5552	0	45.6	45.4	9.0	loam	granular	silasepic
Hougou	C	R5553	0	63.6	35.0	1.4	sandy loam	intertextic	silasepic
Dawaling	A	R5556	0	43.4	37.0	19.6	loam	intertextic	insepic
Dawaling	A	R5557	0	47.6	35.0	17.4	loam	intertextic	Insepic
Dawaling	Bw	R5558	0	62.2	21.8	16.0	sandy loam	granular	silasepic
Dawaling	C	R5560	0	66.8	14.8	18.4	sandy loam	granular	silasepic
Hongshi	above	R5561	0	74.0	18.4	7.6	sandy loam	granular	silasepic
Hongshi	A	R5563	0	18.4	53.6	28.0	silty clay loam	agglomeroplasmic	skelmosepic
Hongshi	Bw	R5564	0	25.6	45.8	28.6	clay loam	porphyroskelic	bimasepic
Hongshi	Bg	R5565	0	23.2	52.6	24.2	silt loam	porphyroskelic	bimasepic
Hongshi	C	R5566	0	50.6	30.8	18.6	loam	granular	silasepic
Jeipan	above	R5567	0	8.8	51.0	40.2	silty clay	porphyroskelic	argillasepic
Jeipan	A	R5568	0	22.2	43.0	34.8	clay loam	porphyroskelic	insepic
Jeipan	C	R5569	0	43.2	35.2	21.6	loam	granular	silasepic
Jeipan	C	R5570	0	16.2	57.4	26.4	silt loam	granular	silasepic
Jeipan	C	R5571	0	72.4	20.4	7.2	sandy loam	granular	silasepic
Wanghua	A	R5572	0	19.6	44.4	36.0	silty clay loam	agglomeroplasmic	skelmosepic
Wanghua	A	R5573	0	29.4	35.8	34.6	clay loam	agglomeroplasmic	skelmosepic
Wanghua	Bw	R5574	0	37.0	39.2	23.8	loam	agglomeroplasmic	isotic
Wanghua	Bw	R5575	0	31.8	46.2	22.0	loam	agglomeroplasmic	isotic
Wanghua	Bw	R5576	0	32.0	47.4	20.6	loam	agglomeroplasmic	insepic
Wanghua	Bw	R5577	0	38.0	47.7	14.2	loam	intertextic	argillasepic
Wanghua	C	R5578	0	1.6	86.6	11.8	silt	intertextic	argillasepic
Wanghua	C	R5579	0	80.6	12.4	7.0	loamy sand	granular	silasepic
Jeipan	A	R5580	0	5.8	79.8	14.4	silt loam	intertextic	insepic
Jeipan	C	R5581	9.0	41.0	41.6	8.4	silt loam	agglomeroplasmic	insepic
Hougou	above	R5582	0	79.8	12.8	7.4	loamy sand	granular	silasepic
Hougou	A	R5583	0	69.8	12.8	17.4	sandy loam	granular	silascpic
Hougou	By	R5586	0	85.8	5.6	8.6	loamy sand	granular	silasepic
Yakou	above	R5589	0	79.4	11.6	9.0	loamy sand	granular	silasepic
Yakou	above	R5590	0	72.0	15.2	12.8	sandy loam	granular	silasepic
Yakou	A	R5591	0	75.6	7.8	16.6	sandy loam	granular	silasepic
Yakou	C	R5592	0	77.2	11.4	11.4	sandy loam	granular	silasepic
Yakou	A	R5593	0	49.8	30.8	19.4	loam	granular	silasepic
Lushan	A	R5594	0	47.0	27.2	25.8	sandy clay loam	porphyroskelic	skelmosepic
Lushan	C	R5595	0	68.6	19.0	12.4	sandy loam	granular	silasepic
Lushan	C	R5596	0	76.4	10.8	12.8	sandy loam	granular	silasepic
Lushan	C	R5597	0	71.2	22.4	6.4	sandy loam	granular	silasepic
Jiepan	C	R5602	0	66.8	15.8	17.4	sandy loam	granular	silasepic
Lushan	A	R5603	0	54.6	22.2	23.2	sandy clay loam	agglomeroplasmic	skelmosepic
Lushan	C	R5605	0	61.6	21.4	17.0	sandy loam	granular	silasepic
Yakou	A	R5609	0	54.6	29.0	16.4	sandy loam	granular	silasepic
Yakou	C	R5610	0	60.4	30.6	9.0	sandy loam	granular	silasepic
Yakou	C	R5611	0	66.2	23.8	10.0	sandy loam	granular	silasepic
Yakou	A	R5612	0	58.8	34.2	14.0	sandy loam	granular	silasepic
Yakou	C	R5613	0	59.4	29.8	10.8	sandy loam	granular	silasepic
Yakou	A	R5614	0	65.2	19.4	15.4	sandy loam	granular	silasepic
Yakou	C	R5615	0	69.4	25.0	5.6	sandy loam	granular	silasepic
Wanan	Bw	R5620	0	62.2	25.6	12.2	sandy loam	intertextic	crystic
Wanan	C	R5621	0	64.2	30.6	5.2	sandy loam	intertextic	crystic
Wanan	R	R5622	0	64.4	32.4	3.2	sandy loam	intertextic	crystic
Wanan	R	R5623	0	65.4	30.6	4.0	sandy loam	intertextic	crystic
Wanan	R	R5624	0	88.6	11.4	0	sand	intertextic	crystic
Xiaoshan	above	R5627	0	60.8	20.0	19.2	sandy loam	intertextic	skelmosepic
Xiaoshan	A	R5628	0	50.2	18.6	31.2	sandy clay loam	agglomeroplasmic	bimasepic
Xiaoshan	C	R5629	0	48.4	31.4	20.2	loam	agglomeroplasmic	skelmosepic
Xiaoshan	C	R5630	0	48.6	34.4	17.0	loam	intertextic	argillasepic
Lushan	above	R5632	0	42.0	44.4	13.6	loam	intertextic	argillasepic
Lushan	A	R5633	0	43.8	37.6	18.6	loam	porphyroskelic	skelmosepic
Jeipan	A	R5634	0	6.4	67.0	26.6	silt loam	prophyroskelic	clinobimasepic
Jeipan	Bw	R5635	0	11.2	66.4	22.4	silt loam	porphryoskelic	insepic
Jeipan	C	R5636	0	9.4	87.2	3.4	silt	intertextic	argillasepic
Jeipan	C	R5637	0	27.6	68.8	3.6	silt loam	intertextic	argillasepic
Lushan	A	R5638	0	12.8	70.8	16.4	silt loam	intertextic	insepic
Lushan	C	R5639	0	8.2	75.0	16.8	silt loam	intertextic	argillasepic
Lushan	C	R5640	0	15.0	76.0	9.0	silt loam	porphyroskelic	argillasepic
Xiaoshan	A	R5641	0	64.4	28.2	13.4	sandy loam	intertextic	insepic

(*continued on next page*)

Table 2 (*continued*)

Pedotype	Hoz	No.	% gravel	% sand	% silt	% clay	Textural class	Grain fabric	Plasmic fabric
Xiaoshan	A	R5642	0	62.4	23.8	13.8	sandy loam	intertextic	Insepic
Xiaoshan	C	R5643	0	64.2	25.6	10.2	sandy loam	intertextic	argillasepic
Xiaoshan	C	R5644	0	56.0	32.4	11.6	sandy loam	intertextic	argillasepic
Xiaoshan	C	R5645	0	79.0	13.6	7.4	loamy sand	intertextic	argillasepic
Daquan	above	R5646	0	53.6	29.2	17.2	sandy loam	intertextic	argillasepic
Daquan	A	R5648	0	40.4	33.2	26.4	loam	agglomeroplasmic	insepic
Lushan	A	R5654	0	12.4	78.8	8.8	silt loam	intertextic	argillasepic
Lushan	C	R5655	0	62.4	28.0	9.6	sandy loam	intertextic	argillasepic

thin section (Fig. 7G). Likely halite (NaCl) casts were also seen in a thin section of a Jiepan profile in the Baicaoping Formation: one of them dissolved and filled from above, and another replaced with quartz (Fig. 7E). Halite hopper casts, with concentric bowed in edges, in the Beidajian Formation, are illustrated by Tang et al. (2011, Fig. 5E). These halite casts were not sand crystals but limpid crystals precipitated, and partly dissolved, at the surface.

Sand crystals form by replacement and cementation without extensive displacement of matrix within the confining pressure of soil, and are commonly known as desert roses (Watson, 1985; Al-Kofahi et al., 1993). As in gypsic horizons of desert soils (Retallack and Huang, 2010), sand crystals are organized into subsurface (By) horizons (Fig. 5). Limpid crystals of halite on the other hand form in marginal marine or lacustrine sabkhas, where precipitation from water or saturated sediment displaces surrounding grains (Renaut and Tiercerlin, 1994; Eriksson et al., 2005; Ziegenbalg et al., 2010).

5.8. Mineral weathering trends

Point counting of individual beds shows a considerable variation in degree of weathering from the surficial depletion of feldspar and rock fragments with increased surficial clay (Figs. 5 and 6). Clay enrichment toward the surface of beds is abruptly truncated below sharp grain size discontinuities with overlying siltstone and sandstone, and clay is confined to intervals only 5–15 cm thick. This is seen especially in profiles with the greatest thickness without clear sedimentary structures, but not in profiles with relict bedding and ripple marks.

Clay enrichment near the surface may thus be due to hydrolytic weathering of feldspar and rock fragments to clay, and this was most marked in profiles with sedimentary structures obscured by physical cracking and chemical weathering. Clayey bed tops do not appear to be part of graded beds such as turbidites deposited in a water column (Komar, 1985; Korsch et al., 1993), for several reasons: their clay content is no more than 40%, bedding is not preserved, color is red and oxidized, and some beds dominated by silt are like loess. Asymmetric enrichment of clay in bed tops over intervals of only 15 cm is unlike symmetrical hydrothermal or diffuse metamorphic alteration (Kelka et al., 2017; Wallace and Hood, 2018).

5.9. Chemical weathering trends

Chemical trends within the beds are quite varied (Figs. 5 and 6). Most profiles have very low soda/potash and alkaline earth/alumina ratios, so were not salinized or calcified, but the Wanan profile is an exception with high soda and carbonate. Alumina/silica and alumina/bases are high in the two profiles (Wanan and Daheitan) on basement rocks below the Ruyang Group, but modest in other profiles, and very low in profiles with a lot of sedimentary structures. Alumina enrichment thus shows trends similar to clay in the mineral weathering trends. Molar weathering ratios do show sharp changes between sedimentary beds, but smooth and subdued trends between bed boundaries. None of the chemical trends are like those of graded beds such as turbidites, which show surface enrichment in alumna, lime and magnesia (Korsch et al., 1993).

5.10. Tau analysis

A definitive method to disentangle soil formation from sedimentation is tau analysis (Brimhall et al., 1992). Tau analysis isolates two separate aspects of weathering: mole fraction mass transport ($\tau_{j,w}$) of a mobile element and mole fraction strain ($\varepsilon_{i,w}$) of an immobile element (Ti used here), using the following formula including bulk density (ρ in g.cm^{-3}) and oxide assay (C in weight %) for successive samples (subscripts i,j) of weathered material (subscript w) and parent material (subscript p).

$$\varepsilon_{i,w} = \left[\frac{\rho_p C_{j,p}}{\rho_w C_{j,w}}\right] - 1 \quad (3)$$

$$\tau_{j,w} = \left[\frac{\rho_w C_{j,w}}{\rho_p C_{j,p}}\right]\left[\varepsilon_{i,w} + 1\right] - 1 \quad (4)$$

Soils and paleosols lose mass with weathering and so have negative strain ($\varepsilon_{i,w} < 0$), and also lose nutrient cations and silica, so have negative mass transfer ($\tau_{j,w} < 0$). In contrast, sediment accumulation and diagenetic alteration adds elements and mass so has positive strain and mass transfer. Tau analysis has been widely used for Precambrian paleosols (Retallack and Mindszenty, 1994; Liivamägi et al., 2014), as well as Cenozoic paleosols (Bestland et al., 1996; Sheldon and Tabor, 2013), and modern soils (Chadwick et al., 1990; Hayes et al., 2019).

From this perspective, the analyzed beds of the Ruyang Group are largely in the negative strain and mass transfer field of soils. An exception is the Dawaling profile, which shows negative strain, but also appreciable gains in Mg and K, in the surface breccia, which is thus probably not a genetic part of that profile. The surface of the Wanghua profile also shows sedimentary addition of material at the top. Depletions of elements in all these paleosols, including the basal disconformity profiles, are modest, suggestive of limited chemical weathering.

6. Paleosol interpretation

6.1. Paleosol identification

The preceding paragraphs outline a variety of paleosol features in the Ruyang Group, but the rest of this paper explores the kinds of paleosols present and their paleoenvironmental implications. The various kinds of beds analyzed as putative paleosols have been given non-genetic names (Table 4) using localities in Henan. These pedotypes can be interpreted in terms of soil taxonomy and various soil-forming factors to build a detailed model of their paleoenvironment (Fig. 10). Hougou profiles with cracked surface (A horizon) over a diffuse horizon with mottles and sand crystals (By or gypsic) are most like Gypsids (Soil Survey Staff, 2014). Wanghua profiles, on the other hand, have deeply cracked surfaces (A horizon) over a slickensided clayey (Bw horizon), as in Vertisols (Soil Survey Staff, 2014). Comparable considerations can be used to classify these paleosols in other classifications (Table 4) of Australia (Stace et al., 1968; Isbell, 1996), and of the Food and Agriculture Organization (1977) and Food and Agriculture Organization (1978). Other profiles are less well developed Entisols and Inceptisols (of Soil Survey Staff, 2014), and would have been restricted to disturbed parts of the landscape (Table 5).

Table 3
Mineral content from point counting thin sections (500 points) of samples from Henan, China

Pedotype	Hoz	No.	% clay	% calcite	% thenardite	% gypsum	% iddingsite	% pyroxene	% rock	% feldspar	% mica	% quartz	% opaque
Daheitan	above	R5539	25.4	0	0	0	0	0	4.4	33.0	1.0	32.0	4.2
Daheitan	A	R5540	8.4	0	0	0	0	2.2	0	54.0	6.8	9.4	19.2
Daheitan	A	R5541	1.6	0	0	0	0	3.0	0	55.0	16.8	9.2	14.4
Daheitan	Bw	R5543	0.6	0	0	0	0	13.2	0	52.4	13.8	7.4	12.4
Hougou	A	R5549	17.2	0	0	0	0	0	2.8	42.8	1.0	34.8	1.4
Hougou	By	R5550	11.6	0	0	4.0	0	0	2.0	39.8	0.6	40.4	1.6
Hougou	By	R5551	12.6	0	0	2.8	0	0	3.4	43.6	1.4	35.0	1.0
Hougou	C	R5552	10.4	0	0	0	0	0	3.2	43.2	1.0	39.4	2.8
Hougou	C	R5553	2.8	0	0	0	0	0	5.4	43.2	2.4	43.6	2.6
Dawaling	A	R5556	23.4	0	6.6	0	0	0	4.2	30.8	2.0	27.4	5.6
Dawaling	A	R5557	17.4	0	5.2	13.4	0	0	1.4	28.8	2.4	29.0	2.4
Dawaling	Bw	R5558	18.2	0	0	0	0	0	2.6	39.4	1.6	36.2	2.0
Dawaling	C	R5560	20.0	0	0	0	0	0	3.0	34.2	0	37.6	5.2
Dawaling	C	R5561	9.6	0	0	0	0	0	3.0	32.0	0.6	49.2	5.6
Hongshi	A	R5563	27.2	0	0	0	0	0	1.2	31.6	10.8	24.0	3.2
Hongshi	Bw	R5564	26.8	0	0	0	0	0	5.2	28.8	5.2	27.2	6.8
Hongshi	Bg	R5565	22.2	0	0	0	0	0	2.8	30.2	10.8	26.0	8.0
Hongshi	C	R5566	19.6	0	0	0	0	0	1.6	36.4	3.8	34.8	3.8
Jeipan	above	R5567	41.4	0	0	0	0	0	0.6	29.2	7.2	20.4	1.2
Jeipan	A	R5568	32.6	0	0	0	0	0	0.8	30.2	7.4	26.0	3.0
Jeipan	C	R5569	23.6	0	0	0	0	0	4.2	32.8	2.0	33.2	4.2
Jeipan	C	R5570	22.6	0	0	0	0	0	1.6	35.4	5.8	32.2	2.4
Jeipan	C	R5571	9.8	0	0	0	0	0	3.0	38.4	2.4	44.6	1.8
Wanghua	A	R5572	37.4	0	0	0	0	0	0.8	29.2	1.6	28.0	3.0
Wanghua	A	R5573	32.0	0	0	0	0	0	0.6	29.8	2.0	31.2	4.4
Wanghua	Bw	R5574	25.4	0	0	0	0	0	3.6	31.0	5.0	30.2	4.8
Wanghua	Bw	R5575	21.8	0	0	0	0	0	3.4	34.4	8.0	29.0	3.4
Wanghua	Bw	R5576	21.6	0	0	0	0	0	7.6	33.2	5.2	27.0	5.4
Wanghua	Bw	R5577	13.6	0	0	0	0	0	13.0	36.0	6.4	26.4	4.6
Wanghua	C	R5578	12.8	0	0	0	0	0	2.6	35.0	17.0	27.2	5.4
Wanghua	C	R5579	7.6	0	0	0	0	0	1.2	40.8	0.6	49.2	0.6
Jeipan	A	R5580	14.0	0	0	0	0	0	0.6	39.8	12.4	29.8	3.0
Jeipan	C	R5582	11.0	0	0	0	0	0	11.6	40.4	0.4	32.4	4.4
Hougou	above	R5582	8.2	0	0	0	0	0	0.6	39.0	0	50.2	2.0
Hougou	A	R5583	19.8	0	0	0	0	0	0.4	37.4	1.8	36.2	4.4
Hougou	By	R5586	6.6	0	0	0	0	0	7.6	38.6	0	44.8	2.4
Yakou	above	R5589	9.6	0	0	0	0	0	3.4	37.8	0.4	43.0	5.8
Yakou	above	R5590	17.0	0	0	0	0	0	3.4	33.2	0.2	44.4	1.8
Yakou	A	R5591	21.8	0	0	0	0	0	2.8	31.0	0	38.6	5.8
Yakou	C	R5592	7.6	0	0	0	0	0	8.4	42.6	1.8	35.8	3.8
Yakou	A	R5593	21.2	0	0	0	0	0	3.8	34.2	1.6	34.2	3.2
Lushan	A	R5594	27.6	0	0	0	0	0	4.0	31.6	0.6	32.4	3.8
Lushan	C	R5595	14.8	0	0	0	0	0	4.4	40.6	2.2	36.0	2.0
Lushan	C	R5596	13.8	0	0	0	0	0	5.0	44.2	2.0	33.6	1.4
Lushan	C	R5597	7.2	0	0	0	0	0	2.8	41.8	2.6	42.6	3.0
Jeipan	C	R5602	18.8	0	0	0	0	0	1.6	34.2	0.2	43.0	2.2
Lushan	A	R5603	23.4	0	0	0	0	0	0.8	29.4	1.6	43.4	1.4
Lushan	C	R5605	18.6	0	0	0	0	0	6.2	33.2	0.6	35.0	6.4
Yakou	A	R5609	17.2	0	0	0	0	0	1.4	32.2	0	47.8	1.4
Yakou	C	R5611	11.2	0	0	0	0	0	3.4	38.2	0	44.4	2.8
Yakou	A	R5612	12.8	0	0	0	0	0	3.8	42.0	0	37.8	3.6
Yakou	C	R5613	10.2	0	0	0	0	0	4.2	39.4	0	43.0	3.2
Yakou	A	R5614	16.8	0	0	0	0	0	3.2	38.2	0	39.0	2.8
Yakou	C	R5615	6.2	0	0	0	0	0	3.2	39.8	0	47.8	3.0
Wanan	Bw	R5620	13.0	0	0	0	4.4	14.2	0	42.2	7.6	16.2	2.4
Wanan	Bw	R5621	5.2	0.2	0	0	5.4	9.2	0	39.2	9.4	26.6	4.6
Wanan	Bk	R5622	4.6	14.4	0	0	1.2	16.0	0	36.8	1.2	23.8	2.0
Wanan	Bk	R5623	5.2	6.4	0	0	5.2	28.2	0	26.2	8.0	18.0	2.8
Wanan	R	R5624	0	0	0	0	5.6	45.2	0	24.6	4.4	17.8	2.4
Xiaoshan	above	R5627	21.2	0	0	0	0	0	2.4	35.6	2.4	31.8	6.6
Xiaoshan	A	R5638	29.4	0	0	0	0	0	3.6	30.6	3.4	28.8	4.2
Xiaoshan	C	R5629	22.8	0	0	0	0	0	4.2	32.8	3.2	31.6	5.4
Xiaoshan	C	R5630	22.4	0	0	0	0	0	5.4	33.2	3.6	31.2	4.2
Lushan	above	R5632	14.2	0	0	0	0	0	4.8	36.0	8.8	30.2	6.0
Lushan	A	R5633	19.2	0	0	0	0	0	7.2	36.0	7.0	27.0	3.6
Jeipan	A	R5634	27.6	0	0	0	0	0	2.4	29.4	13.0	23.2	4.4
Jeipan	Bw	R5635	23.0	0	0	0	0	0	2.2	31.8	16.2	23.0	3.8
Jeipan	C	R5636	3.6	0	0	0	0	0	3.8	33.8	26.0	26.6	6.2
Jeipan	C	R5637	4.4	0	0	0	0	0	4.6	27.8	29.6	28.2	5.4
Lushan	A	R5638	16.4	0	0	0	0	0	2.6	31.4	17.6	27.8	4.2
Lushan	C	R5639	16.4	0	0	0	0	0	2.6	30.0	26.4	20.6	4.0
Lushan	C	R5640	8.0	0	0	0	0	0	9.8	23.6	35.2	19.0	4.4
Xiaoshan	A	R5641	13.2	0	0	0	0	0	5.6	34.2	10.4	28.6	7.6
Xiaoshan	A	R5642	16.8	0	0	0	0	0	2.6	36.8	7.0	32.0	2.6

(*continued on next page*)

Table 3 (*continued*)

Pedotype	Hoz	No.	% clay	% calcite	% thenardite	% gypsum	% iddingsite	% pyroxene	% rock	% feldspar	% mica	% quartz	% opaque
Xiaoshan	C	R5643	11.8	0	0	0	0	0	6.0	36.2	6.0	32.0	8.0
Xiaoshan	C	R5644	14.4	0	0	0	0	0	3.4	38.8	7.4	31.6	4.4
Xiaoshan	C	R5645	8.2	0	0	0	0	0	9.2	38.6	6.2	32.0	5.8
Daquan	above	R5646	19.8	0	0	0	0	0	4.2	33.8	7.6	30.8	3.8
Daquan	A	R5648	26.6	0	0	0	0	0	4.6	32.8	2.6	28.8	4.6
Lushan	A	R5654	10.6	0	0	0	0	0	4.2	36.2	14.4	30.4	4.2
Lushan	C	R5655	10.2	0	0	0	0	0	13.0	38.8	5.4	28.2	4.4

In the FAO map classification (Food and Agriculture Organization, 1977; Food and Agriculture Organization, 1978) the soilscape of the Bingmagou Formation had moderately developed Vertisols (Daquan), and would represent a map code of Vc + Bg, Bk, Rd, Jd. The closest modern match is map unit Vc47-3b + Bk, Bv, I, Le, in the valley near Hama, Syria, under Mediterranean high steppe vegetation and subtropical Mediterranean climate (Food and Agriculture Organization, 1977). At Hama, mean annual temperature is 18.2°C and mean annual precipitation is 330 mm, and mean annual range of precipitation 73 mm, with no precipitation for two summer months of July and August (Merkel, 2020). The soilscape of the Yunmengshan Formation had moderately developed Gypsic Yermosols (Hougou), and would represent a map code of Yy + Vc, Bx, Bd, Jd, Bg. The closest modern match is map unit Yy20-2/3a + I, Yk, in the valley near Ar Raqqah, Syria, under temperate semidesert vegetation and subtropical semiarid Mediterranean climate (Food and Agriculture Organization, 1977). At Ar Raqqah, mean annual temperature is 18.6°C and mean annual precipitation is 179 mm, and mean annual range of precipitation 39 mm, with no precipitation for three summer months of July to September (Merkel, 2020). The soilscape of the Baicoping Formation was again dominated by Vertisols (Wanghua), and would represent a map code of Vc + Bd, Jd, for a return to conditions like map unit Vc47-3b + Bk, Bv, I, Le, near Hama, Syria. The Beidajian Formation has a more limited array of soils in more waterlogged conditions with Gleyic Cambisols (Jeipan) which would represent a map code Bv-Rd, Jd, like Bv15-3b + L0, Vc, E, I, near Nawa, Syria in Mediterranean subtropical semi desert (Food and Agriculture Organization, 1977). Nawa mean annual temperature is 25.4°C and mean annual precipitation is 368 mm, and mean annual range of precipitation 87 mm, with no precipitation for four summer months of June to September (Merkel, 2020).

6.2. Original parent material

The two paleosols on bedrock below the Ruyang Group formed on bedrock schist (Wanan) and basalt (Daheitan). These two profiles are not especially thick, clayey, or deeply weathered, unlike other Precambrian unconformity paleosols with thick saprolite and saprock (Holland, 1984; Liivamägi et al., 2014). Both have common weatherable minerals: iddingsite weathered from olivine, much plagioclase, and common pyroxene remaining in the Wanan profile. The basalt of the Daheitan profile, was not much older than the basal Yunmengshan Formation, because a 3-m-thick basalt flow is 80 m higher within the Yunmengshan is evidence of continued volcanism (Fig. 4B). The Archean schist (3399–2511 Ma) of the Wanan profile is much older than the basal Bingmagou Formation (<1949 Ma: Gao et al., 2006; Zheng et al., 2008; Zheng et al., 2011), and its lack of deep saprolite or saprock may be due to fluvial terrace incision (Retallack and Roering, 2012).

Parent materials of paleosols within the Ruyang Group were quartzofeldspathic gravel and sand of alluvial fans and rivers draining the North-China Archean craton. The proportion of quartz and dominance of orthoclase is evidence that this was a largely granitic terrane, and that schist or rift valley basalt represented below Wanan and Daheitan profiles were not widespread in source areas. A similar provenance is likely for the silt-dominated parts of the Ruyang Group, which were delivered by wind rather than rivers (Section 5.1)

6.3. Reconstructed sedimentary setting

The Ruyang Group was deposited in valleys on the southern slope of North China craton, east of a rift valley filled with basalt of the Xiong'er Group, which opened onto the sea to the current south (Hu et al., 2016), as represented by limestones of the Guandakou Group (Fig. 1). Onlap relationships of the Bingmagou Formation are evidence of paleotopographic relief of more than 500 m (Yue et al., 2018). Away from steep slopes of the rift margin, most of the studied area was hill ranges of granite and gneiss deformed during the Archean, and locally elevated by block faulting flanking the Xiong'er Rift (Peng 2015).

Conglomerates of the Bingmagou Formation have been interpreted as alluvial fans (Meng et al., 2018; Yue et al., 2018), and sandstones of the Yunmengshan Formation represent alluvial coastal plains (Hu et al., 2014). The steep channeled floodplains were in places softened by loess (Section 5.1), which today has distinctive land forms best characterized as "rolling downs" but with steep angle of repose of terraces and erosional gullies near streams, because of their angular silt grains (Zakrzewska, 1963). The shaley Baicaoping Formation was deposited in coastal lakes and lagoons, but there is no clear indication of marine influence until stromatolitic dolostones of the Beidajian Formation (Zheng et al., 2012). Both Baicaoping and Beidajian gray shales have a variety of organic walled microfossils conventionally interpreted as marine plankton (Yin, 1997; Yin et al., 2005; Agić et al., 2017).

Red color, gypsum desert roses, and thenardite-lined vesicular structure are evidence that most of the Ruyang Group paleosols were freely drained, and drab mottles in the surface of the profiles due to burial gleization are evidence that water ftable was not far below many profiles (Retallack, 1991a). Within the alluvial plains, paleosols with thick clayey surface horizons (Daquan), desert roses (Hougou), and deep slickensides (Hongshi, Wanghua) show the least interruption by flooding or other sedimentation, and thus formed on terraces or floodplains distant from streams (Fig. 10). In contrast, sandy and gravelly paleosols with common ripple marks and bedding (Yakou, Lushan, Xiaoshan) may have formed closest to flooding stream channels. Paleosols between these extremes (Jeipan) may have been at intermediate distances from streams on alluvial levees. This leaves one kind of thin sandy paleosol (Xiatang) which was not well drained and oxidized, nor associated with alluvial facies. Xiatang profiles may have been coastal wetlands.

6.4. Time for formation

The time over which individual paleosols form gives information on sediment accumulation rates of sequences of paleosols. Duration of soil formation for Hougou palsosols can be calculated from a chronofunction for modern aridland soils. Abundance of gypsum in a profile (G as % surface area using comparison chart of Terry and Chilingar, 1955) is a metric for age (A in kyrs) in the Negev Desert of Israel ($r^2 = 0.95$, s.e. = ±15, and $p < 0.01$), as follows (Retallack, 2013).

$$A = 3.987G + 5.774 \quad (5)$$

This gypsic chronofunction applied to 11 Hougou paleosols in the Yunmengshan Formation (Table 6) gives durations of 66–105 ± 15 kyr at a level of 70 m to 26 ± 15 kyr at a depth of 940 m. These Statherian paleosols are thus strongly developed, in the usual scale in which Holocene (up to 10 kyr) soils are moderately developed (Retallack, 2019b).

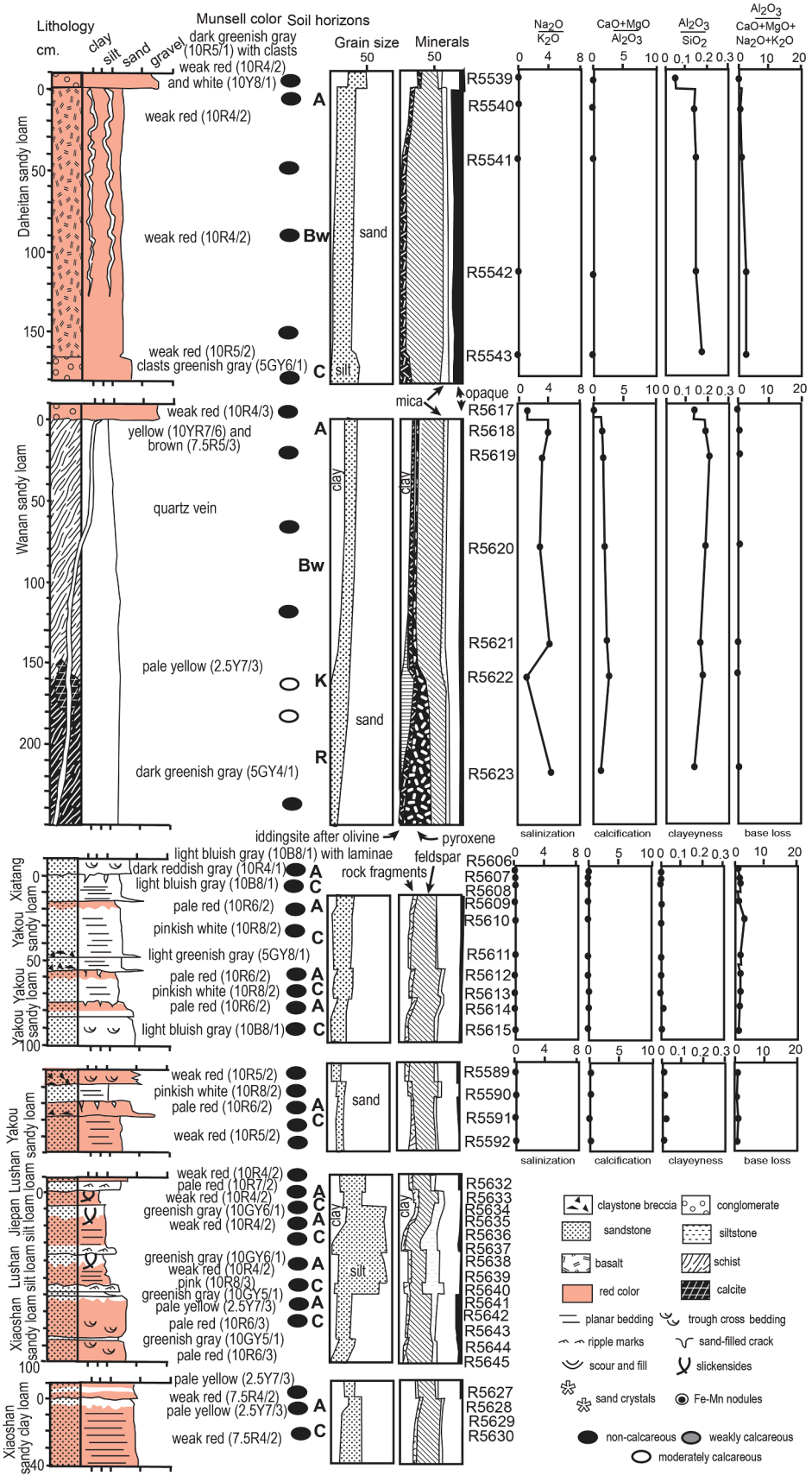

Fig.6. Petrographic and chemical composition of moderately developed paleosols.

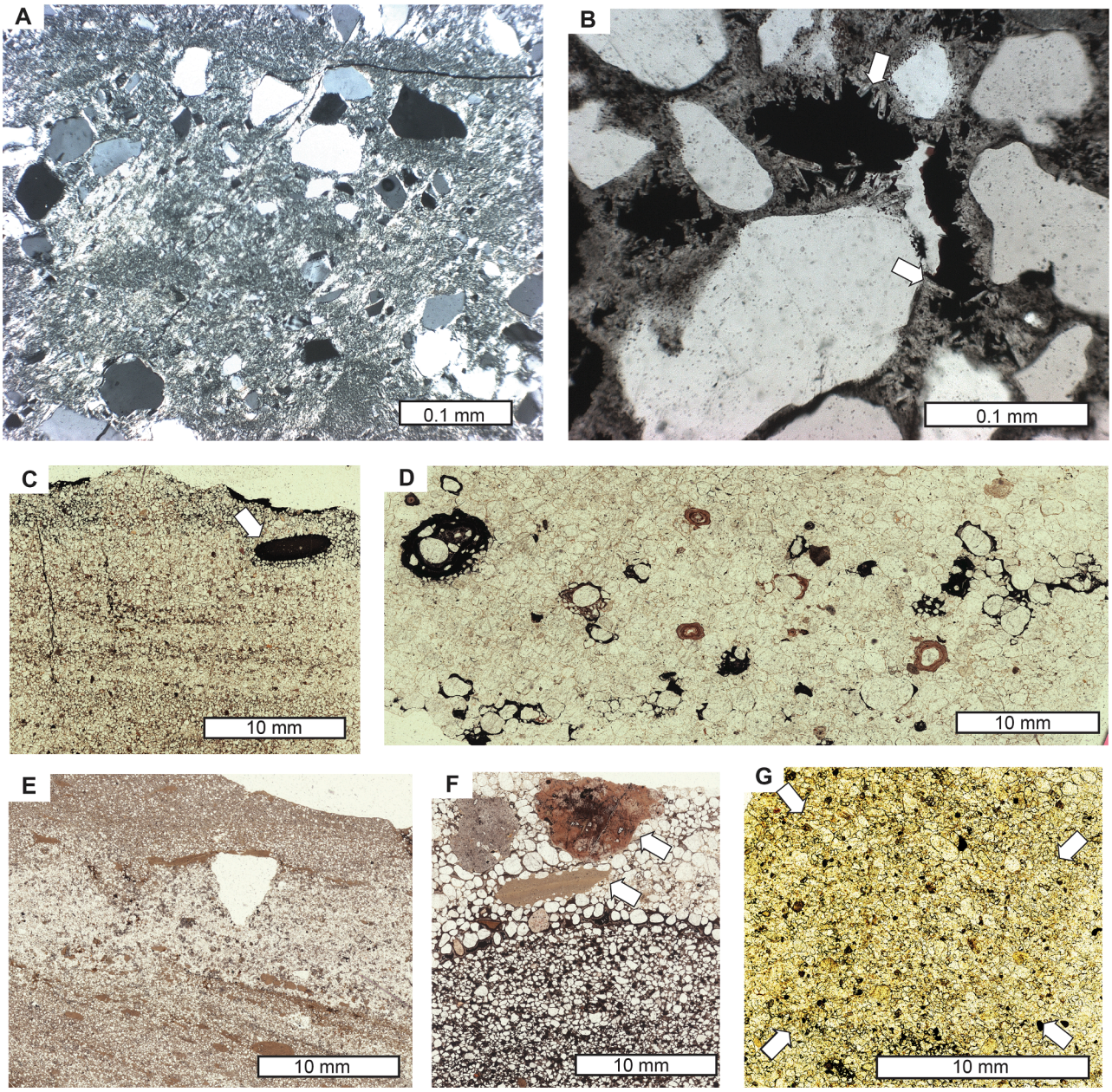

Fig.7. Petrographic thin sections of paleosols (locations hown in Figs. 5 and 6): A, skelmasepic plasmic fabric in A horizon of Wanghua pedotype (R5572); B, thenardite crystals (arrows) lining vesicles filled with birnessite in A horizon of Dawaling pedotype (R5557); C, claystone clast (arrow) and threadlike structures in A horizon of Yakou paleosol (R5566); D, argillans and interconnected birnessite in A horizon of Hougou pedotype (R5583); E, halite casts (right one filled with clear quartz) in A horizon of Jiepan pedotype (R5570); F, red claystone clasts (arrows) in breccia zone atop Dawaling pedotype (R5557), G, radiating pseudomorphs of gypsum of desert rose in By horizon of Hougou pedotype (R5551).

This slowing of sediment accumulation rate in the Yunmengshan Formation was an interlude between more rapid sedimentation of alluvial fans of the Bingmagou Formation and marine transgression of the Baicaoping and Beidajian Fomrtions which have much less developed paleosols.

Another chronofunction developed for bedrock soils of the eastern United States coastal plain (Markewich et al., 1990) derives soil age (A in kyrs) from total profile clay ($r^2 = 0.94$, s.e. $= \pm 12$, and $p < 0.01$)

$$A = 0.136C + 5.865 \quad (6)$$

These calculations give 10,910 years for the Daheitan profile with 37.2 g.cm^{-3} clay and 14,798 years for the Wanan profile with 66.7 g.cm^{-3} clay.

A few millennia are likely for Dawaling, Daquan and Wanghua paleosols with sedimentary structures obscured by cracking to depths of up to 60 cm, and a century or less for Yakou, Lushan, Xiaoshan, and Xiatang paleosols with clear relict bedding. These are maximal estimates, because based on comparison with homogenization of bedding in Pleistocene soils of the San Joaquin Valley, California (Harden, 1982), which were more actively rooted and burrowed than likely for Statherian soils.

6.5. Paleoclimate

Gypsic horizons are today found at depths in soils proportional to mean annual precipitation (Retallack and Huang, 2010). Calcic soils are widespread in aridlands, but gypsic soils form in extreme deserts such as the Atacama Desert of Chile (Navarro-González et al., 2003; Ewing et al.,

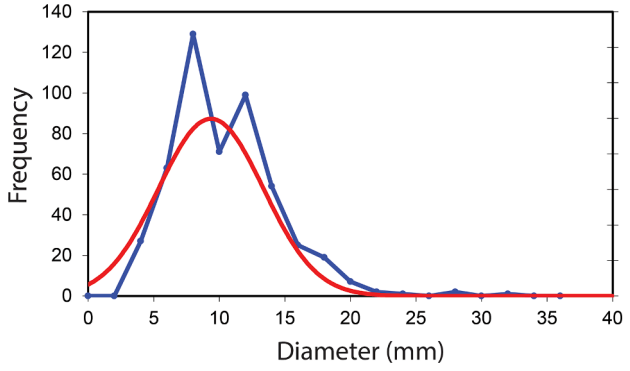

Fig.8. Diameters of desert roses in Hougou pedotype from 530 m in Yunmengshan Formation in Wanghuazhuang section (Fig. 3B). The curve is a computed normal curve for the same mean and standard deviation.

2008). For gypsic soils, another global compilation gives mean annual precipitation from depth to gypsum (D_o again compaction corrected: $r^2 = 0.63$, s.e. = ±129, and $p < 0.00001$), as follows (Retallack and Huang, 2010).

$$P = 87.593e^{0.0209D_o} \quad (7)$$

The gypsic climofunction applied to 11 Hougou paleosols after correcting for compaction using Eq. (2) gives paleoprecipitation of 120 ± 129 mm at a level of 70 m to 152 ± 129 mm at a level of 940 m in the Yunmengshan Formation (Table 6). This trend is not significant because the means and standard deviation for paleoprecipitation of all 11 paleosols are 132 ± 9 mm.

A very different result comes from another paleohyetometer applicable to chemically analyzed paleosols is chemical index of alteration minus potash, because of pervasive K-metasomatism (Novoselov and de Souza Filho, 2015). The CIA-K (*K*) index of paleosol B horizons increases with mean annual precipitation (*P*) according to Eq. (8) (Sheldon et al., 2002: $r^2 = 0.72$, s.e. = ±182, $p < 0.00001$, and is derived from the well-known chemical index of alteration (*I*) of Nesbitt and Young (1982) as a general proxy for the hydrolytic weathering by carbonic acid of feldspar to clay.

$$I = \frac{100(mAl_2O_3)}{[(mAl_2O_3) + (mCaO) + (mNa_2O) + (mK_2O)]} \quad (8)$$

$$P = 221e^{0.0197K} \quad (9)$$

Mean annual precipitation predicted by CIA-K for Ruyang paleosols is much higher than indicated by gypsic depth (Table 6), between 822 and 736 mm (Table 7). This unexpected degree of chemical weathering may be due to acid sulfate weathering, evident from desert roses of Hougou paleosols (Fig. 3B, D), but perhaps promoted by a similar microbiome of sulfur bacteria in other paleosols (Benison et al., 2008). Acid-sulfate weathering is by strong sulfuric acid at pH around 3 (Benison et al., 2007; Benison et al., 2008), unlike modern hydrolytic weathering, which is the basis for CIA and CIA-K, by weak carbonic acid at pH 7 (Nesbitt and Young, 1982). Acid sulfate weathering is uncommon and local today (Benison and Bowen, 2013; Benison and Bowen, 2015) and in the Neoproterozoic (Retallack, 2020), but was widespread in Archean paleosols (Retallack et al., 2016; Retallack, 2018; Retallack and Mao, 2019; Retallack and Noffke, 2019).

Pedogenic paleothermometers based on modern soils of desert (Sheldon et al., 2002) and tundra vegetation (Óskarsson et al., 2012) are preferred to those based on modern woody vegetation (Gallagher and Sheldon, 2013). One of these predicts temperature (*T* in °C) from chemical index of weathering (*W* Eq. (10)), another base depletion metric (Óskarsson et al., 2012), using Eq. (11) ($r^2 = 0.81$, s.e. = ±0.5°C, $p = 0.001$). A second paleothermometer based on modern soils is alkali

Table 4
Pedotypes and diagnosis for Mesoproterozoic red beds of Henan, China

Pedotype	Diagnosis	USDA (Soil Survey Staff 2014)	FAO (1977) and FAO (1978)	CLASSIC (Stace et al. 1968)	AUSTRALIAN (Isbell 1996)
Daheitan	Cracked ferruginized basalt (A) over red clayey basalt (Bw) and basaltic tuff (C)	Ochrept	Dystric Cambisol	Lithosol	Orthic Tenosol
Daquan	Drab mottled red siltstone (A) over slickensided siltstone (Bw) and red bedded siltstone (C)	Ochrept	Chromic Vertisol	Red clay	Brown Vertosol
Dawaling	Red cracked sandstone (A) over red massive sandstone (Bw) and red bedded sandstone (C)	Turbel	Gelic Cambisol	Brown Earth	Dystric Tenosol
Hongshi	Red cracked claystone (A) over deep mukkara structured red claystone (Bw) and gray sandstone (C)	Vertisol	Chromic Vertisol	Red clay	Brown Vertosol
Hougou	Red-green mottled sandstone (A) over red sandstone with large crystal casts (By) and bedded sandstone (C)	Gypsid	Gypsic Yermosol	Solonchak	Brown Sodosol
Jeipan	Red-green mottled claystone (A) over red siltstone (Bw) and gray sandstone (C)	Aquept	Vertic Cambisol	Wiesenboden	Orthic Tenosol
Lushan	Red-green mottled claystone (A) over gray sandstone (C)	Fluvent	Dystric Fluvisol	Alluvial soil	Stratic Rudosol
Wanan	Red claystone (A) over yellow sandy claystone (Bw), calcite cemented hard pan (Bk), and	Calcid	Calcic Cambisol	Lithosol	Calcenic Tenosol

(*continued on next page*)

Table 4 (*continued*)

Pedotype	Diagnosis	USDA (Soil Survey Staff 2014)	FAO (1977) and FAO (1978)	CLASSIC (Stace et al. 1968)	AUSTRALIAN (Isbell 1996)
	green-gray pyroxenite schist (C)				
Wanghua	Green claystone (A) over red slickensided claystone (Bw), and bedded red siltstone (C).	Vertisol	Chromic Vertisol	Brown clay	Brown Vertosol
Xiaoshan	Yellow sandstone (A) over bedded red sandstone (C).	Psamment	Dystric Regosol	Siliceous sand	Arenic Rudosol
Xiatang	Gray cracked siltstone (A) over bedded gray sandstone (C)	Aquent	Dystric Fluvisol	Humic gley	Oxyaaquic Hydrosol
Yakou	Red sandstone with cracks (A) over red bedded sandstone (C)	Psamment	Dystric Regosol	Earthy sand	Arenic Rudosol

index (Sheldon et al., 2002), predicts temperature (T in °C) from the ratio of soda + potash/alumina (M as mole fraction) using Eq. (12) ($r^2 = 0.37$, s.e. = 4.4°, $p < 0.0001$).

$$W = \frac{100(mAl_2O_3)}{[(mAl_2O_3) + (mCaO) + (mNa_2O)]} \quad (10)$$

$$T = 0.21W - -8.93 \quad (11)$$

$$T = -18.5M + 17.3 \quad (12)$$

Both chemical proxies gives temperate mean annual temperature of 9.1 ± 4.4 °C to 11.1 ± 0.5 °C for most of the paleosols, except Wanan which gives different results for each paleobarometer (Table 7). Cool temperatures are also compatible with CIA values of 64–73%, because <65 is found in glacial-frigid climates and greater than 80 in tropical climates (Nesbitt and Young, 1982). This result indicates non-analog Mesoproterozoic climate, because paleomagnetic studies are evidence of tropical paleolatitudes of <10° during deposition of the Ruyang Group between 1740 and 1590 Ma (Zhang et al., 2009; Zhang et al., 2012). Climate modelling of the Mesoproterozoic without polar ice caps gives tropical temperatures of over 30°C at 1520 Ma (Liu et al., 2019). Cooler tropical temperatures estimated here are compatible with climate modelling from CO_2 levels in the Proterozoic atmosphere (Kanzaki and Murakami, 2018b).

6.6. Life on land

Two independent metrics are evidence of microbial life in Ruyang paleosols. Depletion of the essential micronutrient P in paleosols is one indication (Neaman et al., 2005a; Neaman et al., 2005b), and tau analysis (Eqs. (3) and (4)) shows up to 16–59 % surficial depletion of phosphorus (Fig. 9, Table 7). Marine sediments, in contrast, show little change in phosphate with depth or enrichment in phosphate (Filippelli, 2011). A second indication of life in Hougou paleosols is depth to gypsic horizons, corrected for burial compaction (D_o, calculated using Eq. (2)) as a proxy for soil-respired CO_2 (R in ppm: Breecker and Retallack, 2014), using Eq. (12) ($r^2 = 0.64$; S.E. ± 552; $p < 0.05$).

$$R = 35.2D_o + 588 \quad (13)$$

Secondary productivity of CO_2 controls the level at which soluble salts can be precipitated in the soil, and like primary productivity (Retallack and Huang, 2010), is also related to mean annual precipitation (Eq. (6)). These values calculated for Ruyang paleosols are 1031–1521 ± 552 ppm (Table 6), similar to modern microbial gas production in desert soils (Breecker and Retallack, 2014).

A variety of megafossils have been reported from the Ruyang Group. These include stromatolites: *Luoyukouella*, *Lushanella*, and *Parashihsiella* from the marine-influenced Beidajian Formation (Tang et al., 2011). *Ruyangichnus* in the Beidajian Formation (Yang and Zhou, 1995) is a spiral ridge like the aquatic cyanobacterial or algal fossil *Grypania* (Han and Runnegar, 1992). Putative trace fossils in the Beidajian Formation, *Changchengia*, *Torrowangea*, and *Squamodictyo*n (Yang and Zhou, 1995) have also been interpreted as marine animal traces, but are more likely folded mudcrack fills, rather than trace fossils (Zheng and Sun 2011). Putative vermiform trace fossils cf. *Rhysonetron* in the Baicaoping Formation (Hu, 1997) are also like rolled and deformed mudcracks (Zheng and Sun, 2011). These sand-filled cracks in claystone are not as biologically significant as their trace fossil names imply, and are a feature of Lushan paleosols (Fig. 2E). Deformation into spindles of a sort which have been called *Manchuriophycus,* was aided by microbial mats (Cowan and James, 1992). These high relief and overturned examples cases are not subaqueous syneresis (McMahon et al., 2017; Lee et al., 2020).

Microbially induced sedimentary structures (MISS) are also guides to microbial life in paleosols of the Ruyang Group, particularly *Rivularites repertus* (Fig. 11B), a texture of complex intersecting wrinkles and cracks, healed by suturing, as well as gaping (Retallack and Broz, 2020). *Rivularites repertus* is not flexuous, with domes and detached flakes like microbial mats (Noffke, 2010), but matches the biologically mediated shrink-swell patterns of well drained microbial earths (Retallack, 2012a), otherwise known as biological soil crusts (Belnap et al., 2001). Different varieties of MISS from the Ruyang Group represent known variations of biological soil crust (Belnap, 2003), including smooth (Tang et al., 2011, Fig. 6B; Zheng et al., 2016, Fig. 2A), rolling (Yue et al., 2018, Fig. 8G), rugose (Zheng et al., 2016, Fig. 2B), and pinnacled (Tang et al. 2011, Fig. 5F; Zheng et al., 2016, Fig. 4A). These four varieties of biological soil crusts were also observed during our work (Fig. 11).

Below the capping pebbly sandstone of the Dawaling profile discussed in the last section, thin sections reveal millimetric rounded vesicles. The original hollow nature of these is revealed by needles with the orthorhombic form and other mineral properties of thenardite (Na_2SO_4) radiating into the cavity (Fig. 7B). The cavity is now filled by opaque iron-manganese. Vesicular structure (Section 5.4; Fig. 7F) and Fe-Mn rock varnish (Fig. 7C-D) are considered bubbles and precipitates (respectively) of gas from soil microbes (McFadden et al., 1998). Iron- and manganese-oxidizing bacteria are responsible for varnish ministromatolites and vesicle fills, but microbiome studies of these structures in modern soils show that they have a great diversity of bacteria and fungi (Taylor-George et al., 1983; Palmer et al., 1986; Lebedeva et al. 2019).

The exact nature of microbes in paleosols of the Ruyang Group is unknown, but some clues and an evolutionary perspective come from organic microfossils in lacustrine shales of the Ruyang Group, (Yin, 1977; Yin et al., 2005; Yin and Yuan, 2007; Li et al., 2012; Pang et al., 2015; Agić et al., 2017). Filament sheaths may have been cyanobacteria, and large ornamented spheres (such as *Dictyosphaera*) have been considered planktonic algae (Meng et al., 2005; Agić et al., 2017), but fungal affinities have been proposed for both *Tappania* with hyphal extensions (Retallack, 2015b), and chains of *Arctacellularia* (Hermann and Podkovyrov, 2008). These microfossils are in marine or freshwater

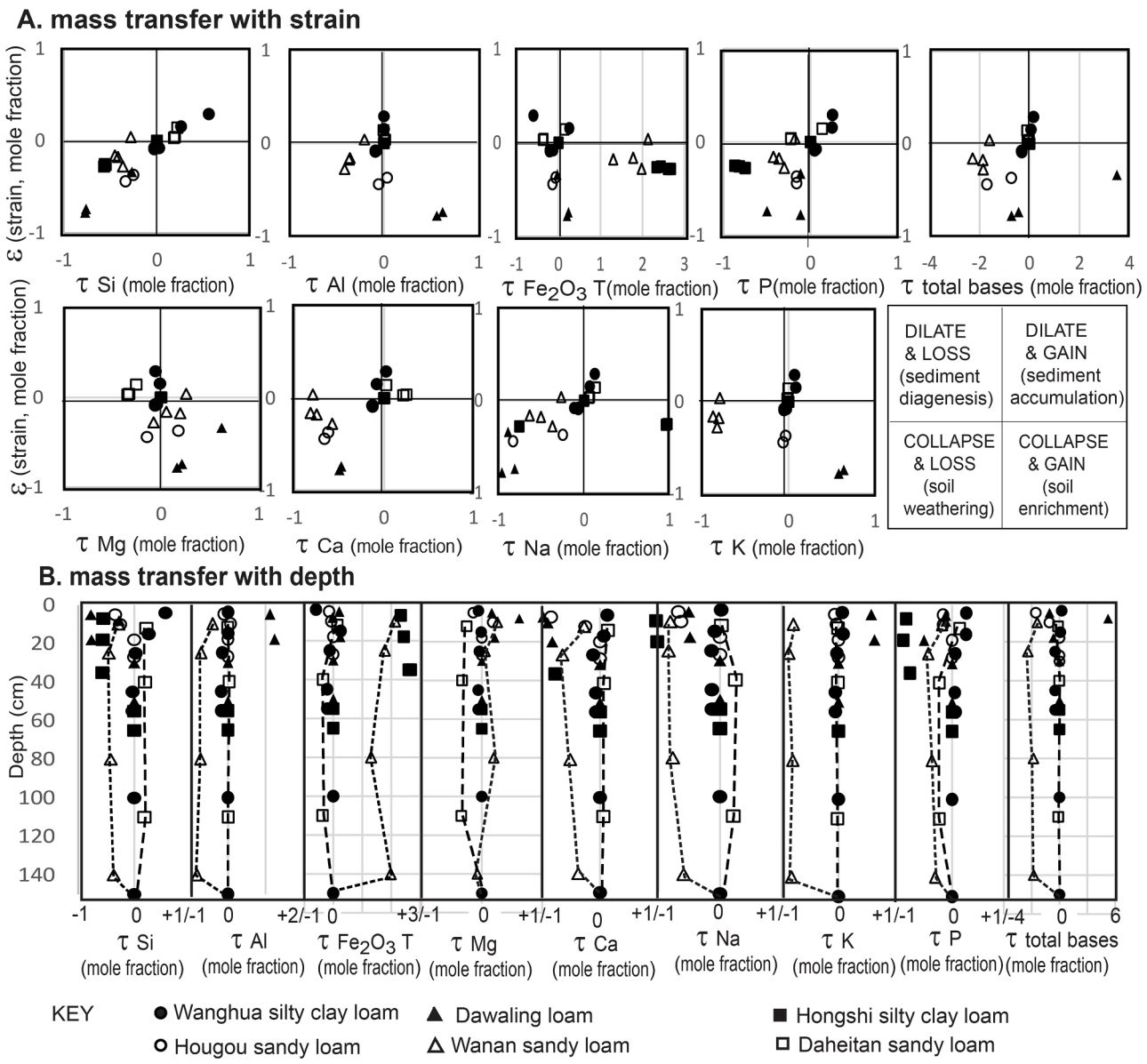

Fig.9. Tau analysis of Mesoproterozoic paleosols of the Ruyang Group.

aquatic shales in the Baicaoping and Beidajian Formations, but prove that these groups had evolved by the Statherian. Cyanobacteria, unicellular algae, and fungi now thrive on land in biological soil crusts (Belnap et al., 2001).

6.7. Atmospheric carbon dioxide

Paleosols of the Ruyang Group show evidence of hydrolytic weathering by carbonic acid, so that the moles of CO_2 used to displace alkali and alkaline earths during weathering assessed by tau analysis (Eqs. (3) and (4)) can be applied to calculate soil CO_2 (ppm) using the paleobarometer of Sheldon (2006), as follows.

$$pCO_2 = \frac{F}{A\left[\frac{K_{CO_2}P}{1000} + \kappa\frac{D_{CO_2}\alpha}{L}\right]} \quad (14)$$

$$F = 2\sum \rho_p \frac{C_{j,p}}{100}\int_{Z=0}^{Z=D_{j,w}} \tau_{j,w(z)}\delta Z \quad (15)$$

Variables needed for these calculations are F (mol CO_2.cm^{-2}) = summed molar mass transfer loss of CaO, MgO, Na_2O and K_2O through the profile using Eq. (14); ρ_p (g.cm^{-3}) = bulk density of parent material; $C_{j,p}$ (weight %) = chemical concentration of an element (j) in parent material (p); $\tau_{j,w}$ (mole fraction) = mass transfer of a specified (j) element in a soil horizon (w); Z (cm) = depth in soil represented by analysis corrected for compaction using Eq. (2); A (years) = duration of soil formation calculated here, in part using Eq. (5); K_{CO2} (mol./kg.bar) = Henry's Law constant for CO_2 (=0.034, range 0.031–0.0045); P (cm) = mean annual precipitation calculated here using Eq. (8); κ (s.cm^3.(mol.year)$^{-1}$) = seconds per year divided by volume per mole of gas at standard temperature and pressure (=1430); D_{CO2} (cm^2.s^{-1}) = diffusion constant for CO_2 in air (=0.162); α (fraction) = ratio of diffusion constant for CO_2 in soil divided by diffusion constant for CO_2 in air (=0.1, range 0.08–0.12); L (cm) = original depth to water table (after decompacted using Eq. (2)). Each one of these variables has its own error, and total error was calculated using Gaussian error propagation in quadrature (Hughes and Hase, 2010). The final value is a likely overestimate for atmospheric CO_2, because of respired CO_2, which in desert soils today is commonly 1000–2000 ppm (3–7 PAL: Breecker and Retallack, 2014), and in modern tropical soils up to 104,000 ppm (371 PAL: Matsumoto

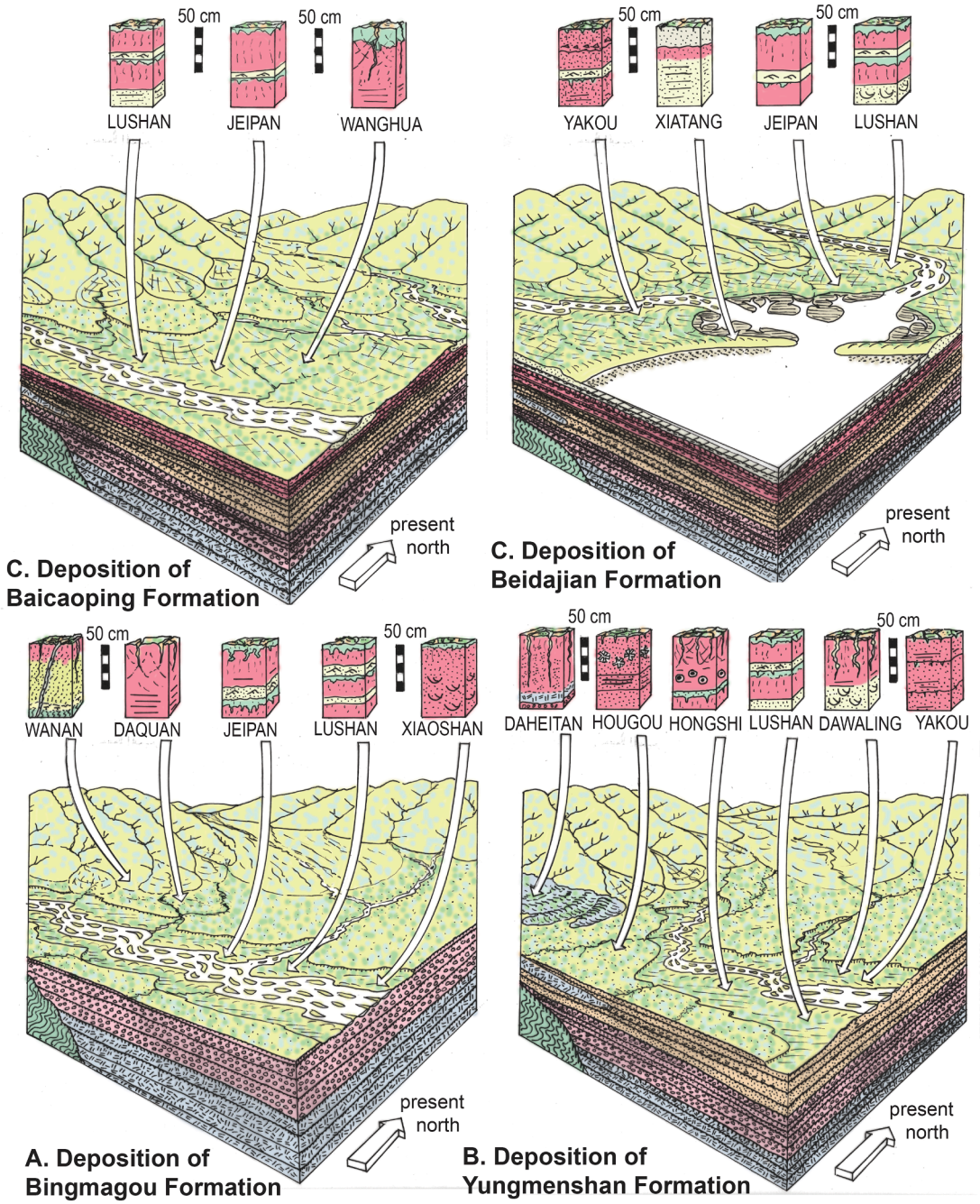

Fig.10. Reconstructions of Mesoproterozoic paleosols of the Ruyang Group.

et al., 1997). Depth to gypsic horizon corrected for burial compaction in the Ruyang Group gives 1031–1521 ± 552 ppm CO_2 of biological productivity for the paleosols using Eq. (13). This low but significant level of respired CO_2 in the paleosols inferred from compaction-corrected depth to Bk, and other evidence for respiring microbial life in the paleosols (Section 6.6), implies that we overestimate atmospheric CO_2 by the respired amount. There is also some uncertainty concerning the fraction of CO_2 present that reacted as acid, implying ours are underestimates of CO_2 (Sheldon et al., 2021). This effect is included in error estimates using temperature-dependent laboratory diffusion constants and other parameters (Sheldon, 2006).

Only a few paleosols of the Ruyang Group are appropriate for this analysis (Table 8), because paleosols with common evaporite minerals formed in part by strong sulfuric acid weathering (Benison and Bowen, 2013) rather than dilute carbonic weathering on which the formulation is based, and other paleosols are not strongly enough developed to reflect atmospheric composition (Sheldon, 2006). The results for soil CO_2 consumption are 1741–20,562 ppm or 6–73 times preindustrial level (PAL), consistent with a theoretical envelope (Fig. 12) of greenhouse gas required to offset a faint young sun (Kasting, 1987; Kanzaki and Murakami, 2018b). Also comparable is a Paleoproterozoic (2.1 Ga) estimate of atmospheric CO_2 of 6440 ± 194 ppm or 23 PAL (Sheldon, 2006) using the same model for the Waterval Onder paleosol (Retallack et al., 2013), 11480 ± 6050 ppm for the 2.69 Ga Alpine Lake paleosol (Driese et al., 2011), 1421 ± 552 ppm for the 1.1 Ga Sturgeon Falls paleosol (Mitchell and Sheldon, 2010). and a different model yielding 1500–9000 ppmv (5–32 PAL) CO_2 for the Archean (3.0 Ga) Jerico Dam paleosol of South Africa (Grandstaff et al., 1986). From this perspective, a recent calculation of 564 ± 46 ppm or 2 PAL CO_2 for a 1.9 Ga paleosol from the Stirling Range Quartzite of Western Australia (Retallack and

Table 5
Interpretation of pedotypes for Mesoproterozoic red beds of Henan, China

Pedotype	Paleoclimate	Ecosystems	Parent Material	Palaeotop-ography	Time for formation (yrs)
Daheitan	Subhumid (769 ± 182 mm MAP), temperate 10.9 ± 4.4oC MAT), seasonally dry	Microbial earth	Basalt flow	Bedrock terrace	10,910 ± 12,000
Daquan	Subhumid (846 ± 182 mm MAP), temperate 8.2 ± 4.4oC MAT), seasonally dry	Microbial earth	Quarztofeld-spathic silt	Alluvial terrace	2000
Dawaling	Subhumid (783 ± 182 mm MAP), temperate 10.9 ± 4.4oC MAT), seasonally dry	Manganese oxidizing bacteria of microbial earth	Quarztofeld-spathic silt	Alluvial terrace	1000
Hongshi	Subhumid (785 ± 182 mm MAP), temperate 10.7 ± 4.4oC MAT), seasonally dry	Microbial earth	Quarztofeld-spathic silt	Low alluvial terrace	2000
Hougou	Arid (120–152 mm MAP), temperate 10.6 ± 4.4°C MAT)	Manganese oxidizing bacteria of microbial earth	Quarztofeld-spathic sand	Near-stream levee	26,000–106,000
Jeipan	Subhumid (736 ± 182 mm MAP), cool temperate 9.9 ± 4.4oC MAT), seasonally dry	Microbial earth	Quarztofeld-spathic silt	Near-stream levee	500
Lushan	Not diagnostic for climate	Microbial earth	Quarztofeld-spathic silt	Near-stream levee	100
Wanan	Subhumid (822 ± 182 mm MAP), warm temperate 15.2 ± 4.4oC MAT), seasonally dry	Microbial earth	Pyroxenite schist	Well drained terrace	14,798±12,000
Wanghua	Subhumid (685 ± 182 mm MAP), cool temperate 8.6 ± 4.4oC MAT), seasonally dry	Microbial earth	Quarztofeld-spathic silt	Near-stream levee	2000
Xiaoshan	Not diagnostic for climate	Microbial earth	Quarztofeld-spathic sand	Near-stream levee	100
Xiatang	Not diagnostic for climate	Microbial earth	Quarztofeld-spathic sand	Near-stream levee	100
Yakou	Not diagnostic for climate	Manganese oxidizing bacteria of microbial earth	Quarztofeld-spathic sand	Near-stream levee	100

Table 6
Petrographic and chemical composition of moderately and weakly developed paleosols.

Location	Coordinates (°N.W)	Lev-el (m)	Age (Ma)	Depth to By (cm)	Thick-ness By (cm)	Cryst-al size (cm)	Crystal density (%)	Burial depth (km)	MAP (mm)	Time (kyr)	Soil CO_2 (ppm)
Hongshi	35.42949, 113.35825	940	1732	19	9	0.9	5	5.600	152	26	1521
Wanghua	33.78270, 112.66037	939	1732	14	13	0.8	9	5.599	132	42	1226
Nanchan	35.51641,113.51419	930	1732	18	14	0.8	10	5.590	148	46	1462
Wanghua	33.78455, 112.66012	890	1735	13	9	1.2	12	5.550	128	54	1165
Wanghua	33.78452, 112.65907	870	1737	13	17	2	15	5.530	128	66	1165
Hongshi	35.42798, 113.35699	840	1739	14	10	0.6	4	5.500	131	22	1223
Hongshi	35.42798, 113.35699	839	1739	13	11	0.7	4	5.499	128	22	1164
Wanghua	33.78927, 112.65822	560	1759	13	9	0.8	10	5.220	127	46	1158
Wanghua	33.79020, 112.65275	530	1761	14	13	1.5	20	5.190	131	86	1215
Daheitan	33.79776, 112.63534	70	1794	14	10	3	25	4.730	130	105	1203
Daheitan	33.79776, 112.63534	70	1794	11	9	1	15	4.730	120	66	1031

Table 7
Paleoclimate inferred from chemical composition of Ruyang Group paleosols, China

Location	Pedotype	Coordinates (N.W)	Level (m)	Age (Ma)	MAP (mm) CIA-K	MAT Calkali	MAT C-CIW	CIA (%)	Tau P (mole fraction)
Wanghuazhuang	Jeipan	33.77592, 112.66504	1980	1657	736	9.9	11.4	70	−0.35
Wanghuazhuang	Wanghua	33.78102, 112.66504	1970	1658	685	8.6	11.0	66	0.06
Wanghuazhuang	Hougou	33.79016, 112.65271	1200	1713	793	10.6	11.1	69	−0.16
Wanghuazhuang	Hongshi	33.79444, 112.6369	1160	1716	785	10.7	11.8	73	0.59
Wanghuazhuang	Dawaling	33.79479, 112.63729	820	1740	783	10.9	11.0	72	−0.50
Wanghuazhuang	Hougou	33.79776, 11,263,534	740	1746	741	9.1	11.1	69	−0.16
Wanghuazhuang	Daheitan	33.79879, 112.63475	670	1751	769	10.9	11.0	71	−0.23
Wananshan	Daquan	34.50724, 112.62098	350	1774	846	8.2	7.4	64	0.07
Wananshan	Wanan	34.50028, 112.62179	0	1799	822	15.2	4.7	64	−0.43

Mao, 2019) now seems too low, and may have been compromised by acid-sulfate weathering evident from gypsum pseudomorphs in the profile. Soil CO_2 is higher than atmospheric CO_2 because of soil respiration (Paw et al., 2006; Elberling et al., 2011). Although Sheldon et al. (2021) assumed zero soil respiration in order to simplify CO_2 estimates, many lines of evidence now support low but significant

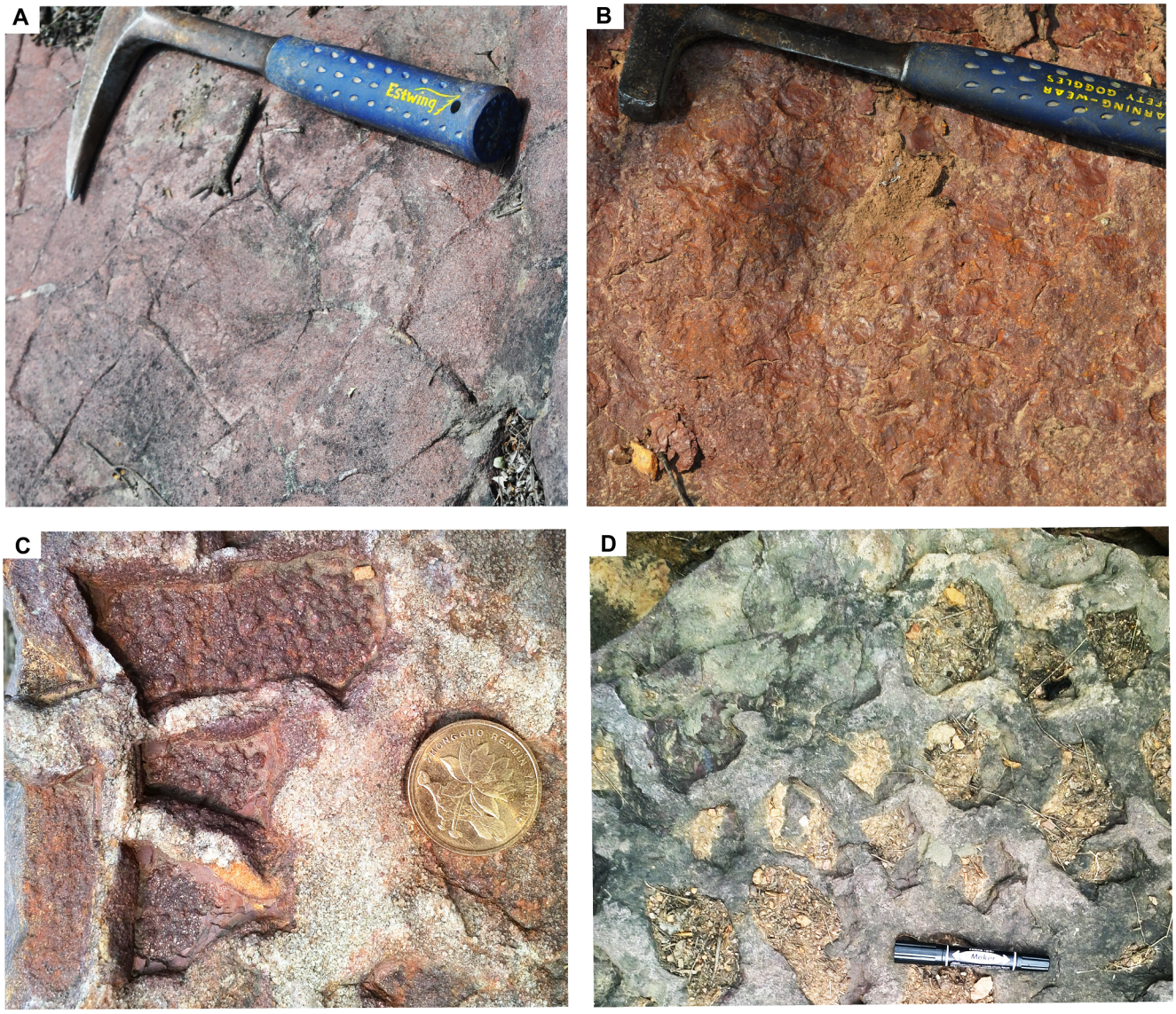

Fig. 11. MISS of the Yunmengshan Formation associated with mudcracks comparable with the modern biological soil crust classification as (A) smooth, (B) rolling, (C) rugose, and (D) pinnacled: A, surface of Yakou pedotype at 550 m in Fig. 4B; B, surface of Hougou pedotype at 470 m in Fig. 4B; C, surface of Dawaling pedotype at 511 m in Fig. 4B; D, surface of Hougou pedotype at 125 m in Fig. 4B.

Table 8
Atmospheric CO_2 and O_2 inferred from paleosols of the Ruyang Group, China

Pedotype	Coordinates (°N.W)	Level (m)	Age (Ma)	MAP (mm)	Format-ion (yrs)	Depth (cm)	CO_2 (ppm)	CO_2 (PAL)	O_2 (ppm)	O_2 (PAL)
Wanghua	33.78102, 112.66504	1025	1700	689	8000	203	1741 ± 818	6 ± 3	16623 ± 87	0.08 ± 0.004
Daheitan	33.79879, 112.63475	670	1751	769	10,910	218	11853 ± 187	42 ± 1	1025 ± 110	0.005 ± 0.0005
Daquan	34.50724, 112.62098	350	1774	846	2000	115	5569 ± 23	20 ± 0.08	2455 ± 38	0.01 ± 0.0002
Wanan	34.50028, 112.62179	0	1799	438	14,798	110	20562 ± 676	73 ± 3	318 ± 295	0.002 ± 0.001

Precambrian soil biomass and respiration (Neaman et al., 2005a; (Neaman et al., 2005b; Retallack et al., 2013; Retallack et al., 2016; Retallack and Mao, 2019).

A different model based on thermodynamics of reconstructed soil minerals by Kanzaki and Murakami (2015) gives higher Paleoproterozoic values (vertical dashed bars in Fig. 12), better aligned with the need for greenhouse gasses to offset the faint young sun (Catling and Kasting 2017). However, in addition to the assumptions about original mineralogy, the Kanzaki and Murakami (2015) results are higher than calculations here because based on temperature of 15°C rather than 9–11°C (Section 6.5), and on dissolution kinetics determined in even warmer laboratory settings (Sheldon et al., 2021). Kanzaki and Murakami (2018a) and Kanzaki and Murakami (2018b) further refine their model and propose that both their and Sheldon's (2006) model define an envelope of possibilities for a cool Proterozoic climate. CO_2 data for the past 600 Ma in Fig. 12A are from a separate theoretical mass balance model of Berner (2006).

Paleoproterozoic CO_2 concentrations<10 PAL are suspect because greenhouse gases are needed to maintain temperate paleotemperatures given a young sun 18–5 % more faint than now over the course of the Proterozoic (Fiorella and Sheldon, 2017). No special pleading is needed for our maximal determinations of atmospheric CO_2 here (Table 8)

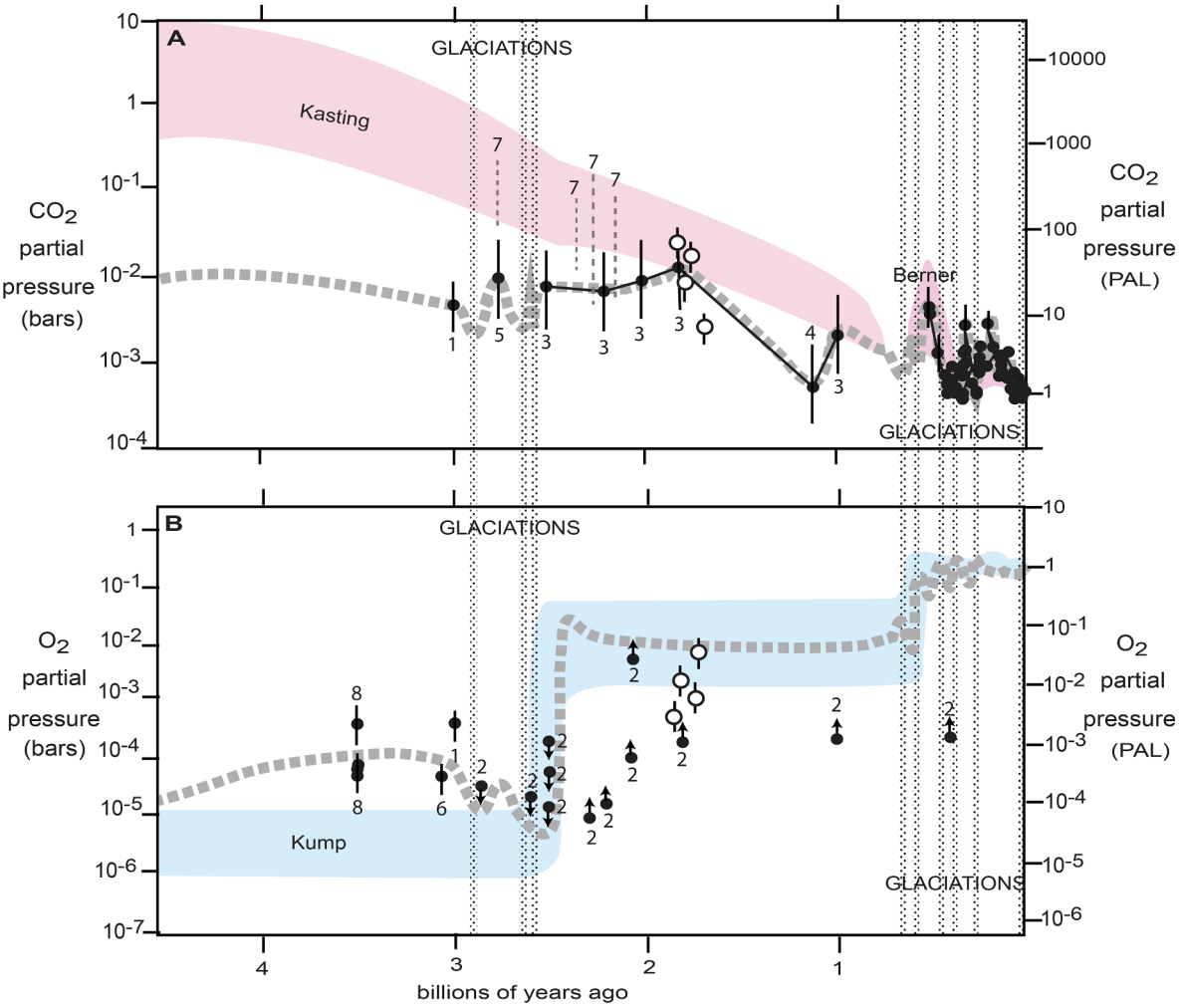

Fig.12. Atmospheric O_2 and CO_2 inferred from paleosols of the 1749–1561 Ma Ruyang Group (open symbols) compared with other Precambrian paleosols (1 = Grandstaff et al., 1986; 2 = Rye and Holland, 1998; 3 = Sheldon, 2006; 4 = Mitchell and Sheldon, 2010; 5 = Driese et al. 2011; 6 = Mukhopadhyay et al., 2014; 7 = Kanzaki and Murakami, 2015; 8 = Retallack 2018), and preferred theoretical envelopes of Kasting (1987) and Kump (2008). Solid circles for past 600 Ma are mass balance model of Berner (2006).

which fall within the envelope needed for greenhouse warming (Fig. 12), but there are other explanations for temperate Proterozoic paleoclimates, even at the equator, which seems to be the case for the Ruyang Group (Zhang et al., 2009; Zhang et al., 2012). There may have been other greenhouse gases, including water vapor, CH_4, C_2H_6, SO_2, and COS (carbonyl sulfide: Kasting and Kirschvink, 2012; Ohmoto et al., 2014). An atmosphere with three times the current mass of N_2 and 10% H_2 may have created an adequate greenhouse (Wordsworth and Pierrehumbert, 2013), but most H_2 would have been converted to CH_4 by methanogenic microbes or escaped to space before the Proterozoic (Catling and Kasting, 2017). Overall atmospheric pressure is another constraint, estimated for the late Archean (2.7 Ga) as <1.1 bars judging from size of raindrop prints (Som et al., 2012), and no greater than 0.5 bars judging from basaltic vesicle sizes at sea level (Som et al., 2016).

6.8. Atmospheric oxygen

Paleosols of the Ruyang Group are also a guide to soil exposure to O_2, and thus partial pressure of atmospheric O_2 (pO_2 in atmospheres). This can be done by modifying the method of Sheldon (2006), using integrated whole profile oxidation of iron and manganese instead of base loss, by Eq. (15) below.

$$pO_2 = \frac{F}{A\left[\frac{K_{O_2}P}{1000} + \kappa\frac{D_{O_2}\alpha}{L}\right]} \quad (16)$$

$$F = 2\sum \rho_p \frac{C_{j,p}}{100}\int_{Z=0}^{Z=D_{j,w}} \tau_{j,w(z)}\delta Z \quad (17)$$

Variables needed for these calculations are F (mol O_2.cm^{-2}) = summed molar mass transfer gains of Fe_2O_3 and MnO through the profile using Eq. (10); ρ_p (g.cm^{-3}) = bulk density of parent material; $C_{j,p}$ (weight %) = chemical concentration of an element (j) in parent material (p); $\tau_{j,w}$ (mole fraction) = mass transfer of a specified (j) element in a soil horizon (w); Z (cm) = depth in soil represented by analysis corrected for burial compaction using Eq. (1); A (years) = duration of soil formation calculated here using Eq. (5); K_{O_2}(mol./kg.bar) = Henry's Law constant for O_2 (=0.00125, range 0.0012–0.0013 from Aachib et al., 2004); P (cm) = mean annual precipitation calculated here using Eq. (8); κ (s.cm^3/mol.year) = seconds per year divided by volume per mole of gas at standard temperature and pressure (=1409); D_{O_2}(cm^2/s) = diffusion constant for O_2 in air (=0.203 at 20°C, range from 0 to 40°C is 0.179–0.227 from Denny, 1993); α (fraction) = ratio of diffusion constant for O_2 in soil divided by diffusion constant for O_2 in air (=0.2, range 0.09–0.32 from Aachib et al., 2004); L (cm) = original depth to

water table (after decompacted using fractional compaction *B*); *B* (fraction) = compaction of Inceptisol due to burial (using Eq. (11) after Sheldon and Retallack, 2001); *k* (km) = depth of burial. Each one of these variables has its own error with total error calculated by Gaussian error propagation (Hughes and Hase, 2010). This method gives precise errors, but that does not mean they are realistic: true errors may be closer to those derived from sensitivity analyses (Sheldon, 2006).

Unlike comparable O_2-demand equations of Holland and Zbiunden (1988), this approach includes bulk density, paleoprecipitation, duration of formation, decompacted thickness, and other constants analogous with Sheldon's (2006) formulation for CO_2 (Eq. (14)). Anaerobic microbial of Mn and Fe requires light as a catalyst and waterlogging, as in banded iron formations (Konhauser et al., 2017; Daye et al., 2019), unlike the crack patterns (Section 5.6) and sand crystals (Section 5.7) deep within Ruyang paleosols. Nor is a primary carbonate pathway facilitating Mn-enrichment (Wittkop et al., 2020), likely in non-calcareous paleosols. Formation of oxidized rock varnish (Section 5.5) is possible in illuminated but anaerobic conditions (Daye et al., 2019), but the method used to estimate O_2 demand here integrates whole profile oxidation, not just surficial crusts. Significant microbial oxidation of Mn and Fe without free oxygen is unlikely considering fungi, cyanobacteria and other aerobic microbes inferred for paleosols and associated lacustrine palynomorphs of the Ruyang Group (Section 6.6). Abiotic and biotic components to overall oxidation of sediments are complex today (Learman et al., 2011), and will be challenging to incorporate in paleosol redox models.

Results for the Ruyang Group (Table 8) are 318–16,623 ppm, which is 0.03–1.6 %, or 0.002–0.08 PAL O_2. Soil O_2 is lower than atmospheric O_2, sometimes by a little in well drained soils (Paw et al., 2006), and sometimes by a lot in waterlogged soils (Vepraskas and Sprecher, 1997; Elberling et al., 2011). The reason for this is soil respiration, which was not zero in our paleosols because of phosphorus depletion and By depth (Section 6.6). Thus, the highest values in the reddest paleosols are a better reflection of atmospheric O_2. Our calculations for paleosols fall within the theoretical range needed (>0.001 PAL) for oxidation of red beds (Kump, 2008; Kump, 2014) and also low O_2 (<0.4 PAL) encouraging sulfide in anoxic Proterozoic oceans (Canfield, 2005). These peculiar Proterozoic oceans are sometimes called "ferruginous oceans" (Poulton and Canfield, 2011), but ferruginous literally means brown in Latin, and is widely used in soil science to describe red or rust colors (Pal et al., 2014). Better names for these odd Proterozoic oceans are "ferrous ocean" (Mikucki et al., 2009) or "Canfield Ocean" (Buick, 2007). Our estimates of O_2 are also compatible with minima indicated by a variety of Proterozoic paleosols (Rye and Holland, 1998). Also within theoretical range is an estimate of 433 ppm (0.002 PAL) O_2 for a 1.9 Ga paleosol from the Stirling Range Quartzite of Western Australia (Retallack and Mao, 2019). These values are much greater than for Archean paleosols (Fig. 11: Grandstaff et al., 1986; Mukhopadhyay et al., 2014). Data for the past 600 Ma in Fig. 12A is from the mass balance model of Berner (2006).

Among other estimates of Proterozoic atmospheric oxygen from marine proxies, such as chromium isotopes in marine shales are contradictory: <0.001 PAL O_2 from 1800 to 800 Ma (Planavsky et al., 2014), <0.01 PAL O_2 from 1600 to 1000 Ma (Cole et al., 2016), but more than 0.01 PAL O_2 from 1459 to 1108 Ma (Canfield et al., 2018). These discrepancies may be from geographic and temporal redox variation in marine shales which formed at varying distances from the atmosphere (Lyons et al., 2014; Diamond et al., 2018). Our result of 0.002–0.08 PAL O_2 (Table 8) is above requirements for eukaryotic cells (0.002 PAL). Only our basal paleosol falls below the requirement for invertebrate animals (0.005–0.04 PAL). Our uppermost paleosol is above requirements for vertebrates (0.05 PAL), and permanent human settlements at high altitude (0.07 PAL: Peacock, 1998; Mills et al., 2014). Our results contradict studies which have linked the rise of metazoa to Late Neoproterozoic atmospheric and ocean oxygenation (Boag et al., 2018; Cole et al., 2020). Furthermore, our measured P-depletion (Fig. 9A; Table 7) and depth to By (Table 6) in these late Paleoproterozoic to early Mesoproterozoic paleosols are comparable with those measured in Ediacaran (Retallack, 2012b), Ordovician (Retallack, 2015c), and arid-land Miocene paleosols (Retallack, 2012b; Retallack, 2015c), suggesting that microbial exploitation of soils and soil respiration were non-zero for all that time. Some studies have assumed that low isotopic or abundance ratios over long periods of time reflect long term anoxia (Cole et al., 2016, Canfield et al., 2018), but perhaps redox instability was more important in hindering metazoan evolution (Johnston et al., 2012). Paleosols can individually give estimates of atmospheric oxygen, and may in future reveal such instabilities, such as the spread of estimates from the Ruyang Group (Table 8). Our results support the conclusion of Mills et al. (2014), that "the origin and earliest evolution of animal life on Earth was not triggered by a rise of atmospheric and marine oxygen in the Neoproterozoic Era…. Instead, other ecological and developmental processes are needed to adequately explain the origin and earliest evolution of animal life on Earth."

7. Conclusions

Paleosols of the Ruyang Group (1749–1561 Ma) in central China formed at the outset of the so called "boring billion" (1800–800 Ma) of Paleoproterozoic to Mesoproterozoic time. Marine rocks of that age are monotonous sulfidic shaley facies, but terrestrial facies and paleosols were as varied and colorful as Phanerozoic paleosol sequences. Distinct associations of named pedotypes were found in alluvial fan facies of the Bingmagou Formation, in fluvial facies of the Yunmengshan Formation, in coastal plain facies of the Baicaoping Formation, and in the coastal to intertidal Beidajian Formation. Hyperarid paleoclimate was cool temperate. The paleosols were alive with iron- and manganese-fixing bacteria that created desert varnish and vesicular structure, as well as sulfur-oxidizing bacteria creating desert roses of gypsum. Combined atmospheric and soil CO_2 mean levels experienced during weathering can be calculated from mass balances as 1741–20,562 ppm (6–73 times preindustrial level or PAL) of atmospheric CO_2, consistent with the amount needed for a greenhouse effect to offset a faint young sun. A similar model indicates no more than 318–16,623 ppm (0.002–0.08 PAL) O_2. This was more than enough to support animals, as much as a billion years before they evolved for reasons other than atmospheric oxidation.

Declaration of Competing Interest

The authors declare that they have no known competing financial interests or personal relationships that could have appeared to influence the work reported in this paper.

Acknowledgments

Ilya Bindeman, Malcolm Walter, Jim Kasting, Nathan Sheldon, Lee Kump, and Roger Buick offered useful discussion. Bin Hu, Deshun Zheng, Wei Zheng, and Fengbo Sun helped with fieldwork. Retallack thanks Hongfu Yin and Shucheng Xie, and other organizers of the 3rd International Conference of Geobiology in Wuhan for travel funding. This study was partly supported by a National Key R & D Program of China grant (2017YFC0603103). Detailed review of the manuscript by Jim Kasting was greatly appreciated.

References

Aachib, M., Mbonimpa, M., Aubertin, M., 2004. Measurement and prediction of the oxygen diffusion coefficient in unsaturated media with applications to soil covers. Water Air Soil Pollut. 156, 163–193.

Agić, H., Moczydłowska, M., Yin, L., 2017. Diversity of organic-walled microfossils from the early Mesoproterozoic Ruyang Group, North China Craton – a window into the early eukaryote evolution. Precambr. Res. 297, 101–130.

Al-Kofahi, M.M., Hallak, A.B., Al-Juwair, H.A., Saafin, A.K., 1993. Analysis of desert rose using PIXE and RBS techniques. X-Ray Spectrom. 22, 23–27.
Allen, C.C., 1978. Desert varnish of the Sonoran Desert: optical and electron probe microanalysis. J. Geol. 86, 743–752.
Álvaro, J.J., Van Vliet-Lanoë, B., Vennin, E., Blanc-Valleron, M.M., 2003. Lower Cambrian paleosols from the Cantabrian Mountains (northern Spain): a comparison with Neogene-Quaternary estuarine analogues. Sed. Geol. 163, 67–84.
Aubele, J.C., Crumpler, L.S., Elston, W.E., 1988. Vesicle zonation and vertical structure of basalt flows. J. Volcanol. Geoth. Res. 35, 349–374.
Belnap, J., 2003. Comparative structure of physical and biological soil crusts. In: Belnap, J., Lange, O.L. (Eds.), Biological Soil Crusts: Structure, Function and Management. Springer, Berlin, pp. 177–191.
Belnap, J., Kaltenecker, J.H., Rosentreter, R., Williams, J., Leonard, S., Eldridge, D., 2001. Biological soil crusts: ecology and management. Bur. Land Manage. Techn. Ref. 1730, 1–110.
Benison, K.C., Bowen, B.B., 2013. Extreme sulfur-cycling in acid brine lake environments of Western Australia. Chem. Geol. 351, 154–167.
Benison, K.C., Bowen, B.B., 2015. The evolution of end-member continental waters: the origin of acidity in southern Western Australia. GSA Today 25 (6), 1–10.
Benison, K.C., Bowen, B.B., Oboh-Ikuenobe, F.E., Jagniecki, E.A., LaClair, D.A., Story, S. L., Mormile, M.R., Hong, B.-Y., 2007. Sedimentology of acid saline lakes in southern Western Australia: newly described processes and products of an extreme environment. J. Sedim. Res. 77 (5), 366–388.
Benison, K.C., Jagniecki, E.A., Edwards, T.B., Mormile, M.R., Storrie-Lombardi, M.C., 2008. "Hairy blobs:" microbial suspects preserved in modern and ancient extremely acid lake evaporites. Astrobiology 8, 1–15.
Berner, R.A., 2006. GEOCARBSULF: a combined model for Phanerozoic atmospheric O_2 and CO_2. Geochim. Cosmochim. Acta 70, 5653–5664.
Bestland, E.A., Retallack, G.J., Rice, A.E., Mindszenty, A., 1996. Late Eocene detrital laterites in central Oregon: mass balance geochemistry, depositional setting and landscape evolution. Geol. Soc. Amer. Bull. 108, 285–302.
Bettis, E.A., Mason, J.P., Swinehart, J.B., Miao, X.-D., Hanson, P.R., Goble, R.J., Loope, D.B., Jacobs, P.M., Roberts, H.M., 2003. Cenozoic eolian sedimentary systems of the USA mid-continent. In: Easterbook, D.J. (Ed.), Quaternary geology of the United States. INQUA field guide volume. Desert Research Institute, Reno, pp. 195–218.
Boag, T.H., Stockey, R.G., Elder, L.E., Hull, P.M., Sperling, E.A., 2018. Oxygen, temperature and the deep-marine stenothermal cradle of Ediacaran evolution. Proc. R. Soc. B 285, 20181724.
Breecker, D.O., Retallack, G.J., 2014. Refining the pedogenic carbonate atmospheric CO_2 proxy and application to Miocene CO_2. Palaeogeogr. Palaeoclim. Palaeoec. 406, 1–8.
Brimhall, G.H., Chadwick, O.A., Lewis, C.J., Compston, W., Williams, I.S., Danti, K.J., Dietrich, W.E., Power, M.E., Hendricks, D., Bratt, J., 1992. Deformational mass transport and invasive processes in soil evolution. Science 255, 695–702.
Buick, R., 2007. Did the Proterozoic 'Canfield Ocean' cause a laughing gas greenhouse? Geobiology 5, 97–100.
Buick, R., Des Marais, D.J., Knoll, A.H., 1995. Stable isotopic compositions of carbonates from the Mesoproterozoic Bangemall Group, northwestern Australia. Chem. Geol. 123, 153–171.
Canfield, D.E., 2005. The early history of atmospheric oxygen: homage to Robert M. Garrels. Annu. Rev. Earth Planet. Sci. 33, 1–36.
Canfield, D.E., Zhang, S., Frank, A.B., Wang, X., Wang, H., Su, J., Ye, Y., Frei, R., 2018. Highly fractionated chromium isotopes in Mesoproterozoic-aged shales and atmospheric oxygen. Nat. Commun. 9, 1–11.
Catling, D.C., Kasting, J.F., 2017. Long-term climate evolution. In: Catling, D.C., Kasting, J.F. (Eds.), Atmospheric Evolution on Inhabited and Lifeless Worlds. Cambridge Univ. Press, Cambridge, pp. 299–326.
Chadwick, O.A., Brimhall, G.H., Hendricks, D.M., 1990. From a black to a gray box—a mass balance interpretation of pedogenesis. Geomorphology 3, 369–390.
Cole, D.B., Reinhard, C.T., Wang, X., Gueguen, B., Halverson, G.P., Gibson, T., Hodgskiss, M.S., McKenzie, N.R., Lyons, T.W., Planavsky, N.J., 2016. A shale-hosted Cr isotope record of low atmospheric oxygen during the Proterozoic. Geology 44, 555–558.
Cole, D.B., Mills, D.B., Erwin, D.H., Sperling, E.A., Porter, S.M., Reinhard, C.T., Planavsky, N.J., 2020. On the coevolution of surface oxygen levels and animals. Geobiology 18, 260–281.
Cowan, C.A., James, N.P., 1992. Diastasis cracks: mechanically generated synaeresis-like cracks in Upper Cambrian shallow water oolite and ribbon carbonates. Sedimentology 39, 1101–1118.
Dalrymple, R.W., Narbonne, G.M., Smith, L., 1985. Eolian action and the distribution of Cambrian shales in North America. Geology 13, 607–610.
Daye, M., Klepac-Ceraj, V., Pajusalu, M., Rowland, S., Farrell-Sherman, A., Beukes, N., Tamura, N., Fournier, G., Bosak, T., 2019. Light-driven anaerobic microbial oxidation of manganese. Nature 576, 311–314.
Denny, M.W., 1993. In: Air and Water: The Biology and Physics of Life's Media. Princeton Univ. Press, Princeton, p. 343.
Diamond, C.W., Planavsky, N.J., Wang, C., Lyons, T.W., 2018. What the ~1.4 Ga Xiamaling Formation can and cannot tell us about the mid-Proterozoic ocean. Geobiology 16, 219–236.
Dorn, R.I., Oberlander, T.M., 1982. Rock varnish. Progr Phys. Geogr. 6, 317–367.
Driese, S.G., Simpson, E.L., Eriksson, K.A., 1995. Redoximorphic paleosols in alluvial and lacustrine deposits, 1.8 Ga Lochness Formation, Mount Isa, Australia; pedogenic processes and implications for paleoclimate. J. Sediment. Res. 65, 675–689.
Driese, S.G., Jirsa, M.A., Ren, M., Brantley, S.L., Sheldon, N.D., Parker, D., Schmitz, M., 2011. Neoarchean paleoweathering of tonalite and metabasalt: implications for reconstructions of 2.69 Ga early terrestrial ecosystems and paleoatmospheric chemistry. Precambr. Res. 189, 1–17.
Elberling, B., Askaer, L., Jørgensen, C.J., Kühl, H.P., Glud, R.N., Lauritsenet, F.R., 2011. 2011, Linking soil O_2, CO_2, and CH_4 concentrations in a wetland soil: implications for CO_2 and CH_4 fluxes. Environ. Sci. Technol. 45, 3393–3399.
Elmore, R.D., 1984. The Copper Harbor Conglomerate: a late Precambrian fining-upward alluvial fan sequence in northern Michigan. Geol. Soc. Amer. Bull. 95, 610–617.
Eriksson, K.A., Simpson, E.L., Master, S., Henry, G., 2005. Neoarchaean (c. 2.58 Ga) halite casts: implications for palaeoceanic chemistry. J. Geol. Soc. London 162, 789–799.
Ewing, S.A., MacAlady, J.L., Warren-Rhodes, K., McKay, C.P., Amundson, R., 2008. Changes in the soil C cycle at the arid-hyperarid transition in the Atacama Desert. J. Geophys. Res. Biogeosci. 113, G02S90.
Filippelli, G.M., 2011. Phosphate rock formation and marine phosphorus geochemistry: the deep time perspective. Chemosphere 84, 759–766.
Fiorella, R.P., Sheldon, N.D., 2017. Equable end Mesoproterozoic climate in the absence of high CO_2. Geology 45, 231–234.
Food and Agriculture Organization, 1977. Soil map of the World 1:5,000,000. Vol. VIII. South Asia. UNESCO, Paris, 117 p.
Food and Agriculture Organization, 1978. Soil map of the World 1:5,000,000. Vol. VIII. North and Central Asia. UNESCO, Paris, 165 p.
Gallagher, T.M., Sheldon, N.D., 2013. A new paleothermometer for forest paleosols and its implications for Cenozoic climate. Geology 41, 647–650.
Gao, L.-Z., Zhao, T., Wan, Y.-S., Zhao, X., Ma, Y.-S., Yang, S.Z., 2006. Report on 3.4 Ga shrimp zircon age from the Yuntaishan Geopark in Jiaozuo, Henan Province. Acta Geol. Sin. Engl. Ed. 80, 52–57.
Garvie, L.A.J., Burt, D.M., Buseck, P.R., 2008. Nanometer-scale complexity, growth, and diagenesis in desert varnish. Geology 36, 215–218.
Gibson, E.K., Wentworth, S.J., McKay, D.S., 1983. Chemical weathering and diagenesis of a cold desert soil from Wright Valley, Antarctica: an analog of Martian weathering processes. J. Geophys. Res. Solid Earth 88, A912–A928.
Grandstaff, D.E., Edelman, M.J., Foster, R.W., Zbinden, E.M., Kimberley, M.M., 1986. Chemistry and mineralogy of Precambrian paleosols at the base of the Dominion and Pongola Groups (Transvaal, South Africa). Precambr. Res. 32, 97–131.
Hamdi-Aissa, B., Vallès, V., Aventurier, A., Ribolzi, O., 2004. Soils and brine geochemistry and mineralogy of hyperarid desert playa, Ouargla Basin, Algerian Sahara. Arid Land Res. Manage. 18, 103–126.
Han, T.M., Runnegar, B., 1992. Megascopic eukaryotic algae from the 2.1-billion-year-old Negaunee Iron-Formation, Michigan. Science 257, 232–235.
Harden, J.W., 1982. A quantitative index of soil development from field descriptions: examples from a chronosequence in central California. Geoderma 28, 1–28.
Hayes, J.L., Riebe, C.S., Holbrook, S.W., Flinchum, B.A., Hartsough, P.C., 2019. Porosity production in weathered rock: Where volumetric strain dominates over chemical mass loss. Sci. Adv. 5, 1–12.
Hermann, T.N., Podkovyrov, V.N., 2008. On the nature of the Precambrian microfossils *Arctacellularia* and *Glomovertella*. Paleontol. J. 42, 655–664.
Holland, H.D., 1984. In: The Chemical Evolution of the Atmosphere and Oceans. Princeton University Press, p. 582.
Holland, H.D., Zbiunden, E.A., 1988. Paleosols and the evolution of the atmosphere: part 1. In: Lerman, A., Meybeck, M. (Eds.), Physical and Chemical Weathering in Geochemical Cycles. Reidel, Dordrecht, pp. 61–82.
Hu, G., Zhao, T., Zhou, Y., 2014. Depositional age, provenance and tectonic setting of the Proterozoic Ruyang Group, southern margin of the North China Craton. Precambr. Res. 246, 296–318.
Hu, J.-M., 1997. Vermiform trace fossils from the Precambrian Ruyang Group, western Henan. Chinese Sci. Bull. 42, 251–254.
Hu, J.-M., Li, Z.-H., Gong, W.-B., Hu, G.-H., Dong, X.P., 2016. Meso-Neoproterozoic stratigraphic and tectonic framework of the North China Craton. In: Zhai, M., Zhao, Y., Zhao, T. (Eds.), Main Tectonic Events and Metallogeny of the North China Craton. Springer Geology Springer, Singapore, pp. 393–417.
Huang, X., Zhang, Z., Zhou, H.R., Liu, Q.J., 2010. Microbial induced sedimentary structures (MISS) of the Mesoproterozoic Ruyang Group in western Henan Province. Geol. China 37, 1399–1404.
Hughes, I., Hase, I.P.A., 2010. In: Measurements and Their Uncertainties: A Practical Guide to Modern Error Analysis. Oxford Univ Press, Oxford, p. 136.
Isbell, R.F., 1996. In: The Australian Soil Classification, revised edition. CSIRO Publishing, Collingwood, p. 144.
Johnston, D.T., Poulton, S.W., Goldberg, T., Sergeev, V.N., Podkovyrov, V., Vorob'eva, N.G., Bekker, A., Knoll, A.H., 2012. Late Ediacaran redox stability and metazoan evolution. Earth Planet. Sci. Lett. 335, 25–35.
Kanzaki, Y., Murakami, T., 2015. Estimates of atmospheric CO_2 in the Neoarchean-Paleoproterozoic from paleosols. Geochim. Cosmochim. Acta 159, 190–219.
Kanzaki, Y., Murakami, T., 2018a. Effects of atmospheric composition on apparent activation energy of silicate weathering: I. Model formulation. Geochim Cosmochim. Acta 233, 159–186.
Kanzaki, Y., Murakami, T., 2018b. Effects of atmospheric composition on apparent activation energy of silicate weathering: II. Implications for evolution of atmospheric CO_2 in the Precambrian. Geochim. Cosmochim. Acta 240, 314–330.
Kasting, J.F., 1987. Theoretical constraints on oxygen and carbon dioxide concentrations in the Precambrian atmosphere. Precambr. Res. 34, 205–229.
Kasting, J., Kirschvink, J., 2012. Evolution of a habitable planet. In: Impey, C., Lunine, J., Funes, J. (Eds.), Frontiers of Astrobiology. Cambridge Univ. Press, New York, pp. 115–131.
Kelka, U., Veveakis, M., Koehn, D., Beaudoin, N., 2017. Zebra rocks: compaction waves create ore deposits. Sci. Rep. 7 (1), 1–9.

Kim, S.B., Chough, S.K., Chun, S.S., 1995. Bouldery deposits in the lowermost part of the Cretaceous Kyokpori Formation, SW Korea: cohesionless debris flows and debris falls on a steep-gradient delta slope. Sed. Geol. 98, 97–119.
Kokelj, S.V., Pisaric, M.F.J., Burns, C.R., 2007. Cessation of ice-wedge development during the 20th century in spruce forests of eastern Mackenzie Delta, Northwest Territories, Canada. Canad. J. Earth Sci. 44, 1503–1515.
Komar, P.D., 1985. The hydraulic interpretation of turbidites from their grain sizes and sedimentary structures. Sedimentology 32, 395–407.
Konhauser, K.O., Planavsky, N.J., Hardisty, D.S., Robbins, L.J., Warchola, T.J., Haugaard, R., Lalonde, S.V., Partin, C.A., Oonk, P.B.H., Tsikos, H., Lyons, T.W., 2017. Iron formations: a global record of Neoarchaean to Palaeoproterozoic environmental history. Earth Sci. Rev. 172, 140–177.
Korsch, R.J., Roser, B.P., Kamprad, J.L., 1993. Geochemical, petrographic and grain-size variations within single turbidite beds. Sed. Geol. 83, 15–35.
Krinsley, D., Dorn, R., Tovey, N.K., 1995. Nanometer-scale layering in rock varnish: implications for genesis and paleoenvironmental interpretation. J. Geol. 103, 106–113.
Kump, L.R., 2008. The rise of atmospheric oxygen. Nature 451, 277–278.
Kump, L.R., 2014. Hypothesized link between Neoproterozoic greening of the land surface and the establishment of an oxygen-rich atmosphere. Proc. Nat. Acad. Sci. 111, 14062–14065.
Lan, Z., Li, X., Chen, Z.Q., Li, Q., Hofmann, A., Zhang, Y., Zhong, Y., Liu, Y., Tang, G., Ling, X., Li, J., 2014. Diagenetic xenotime age constraints on the Sanjiaotang Formation, Luoyu Group, southern margin of the North China Craton: Implications for regional stratigraphic correlation and early evolution of eukaryotes. Precambr. Res. 251, 21–32.
Learman, D.R., Wankel, S.D., Webb, S.M., Martinez, N., Madden, A.S., Hansel, C.M., 2011. Coupled biotic–abiotic Mn (II) oxidation pathway mediates the formation and structural evolution of biogenic Mn oxides. Geochim. Cosmochim. Acta 75, 6048–6063.
Lebedeva, M.P., Golovanov, D.L., Shishkov, V.A., Ivanov, A.L., Abrosimov, K.N., 2019. Microscopic and tomographic studies for interpreting the genesis of desert varnish and the vesicular horizon of desert soils in Mongolia and the USA. Bol. Sociedad Geol. Mexicana 71, 21–42.
Lee, D.C., Byun, U.H., Kwon, Y.K., Keehm, Y., Jeong, G.Y., Yi, K., 2020. *Manchuriophycus*-like elliptical cracks in thin mudstones intercalated with lacustrine sandstone: intrastratal crack formation in water-saturated sediments. Sediment. Geol. 105769.
Li, M., Liu, P.J., Yin, C.Y., Tang, F., Gao, L.Z., Chen, S.M., 2012. Acritarchs from the Baicaoping Formation (Ruyang Group) of Henan. Acta Palaeont. Sinica 51, 76–87.
Li, X.Y., Li, S., Wang, T.S., Dong, Y., Liu, X.G., Zhao, S.J., Wang, K., Sun, J.P., Dai, L.M., Suo, Y.H., 2020. Geochemistry and detrital zircon records of the Ruyang-Luoyu groups, southern North China Craton: Provenance, crustal evolution and Paleo-Mesoproterozoic tectonic implications. Geosci. Frontiers 11, 679–696.
Liivamägi, S., Somelar, P., Mahaney, W.C., Kirs, J., Vircava, I., Kirsimäe, K., 2014. Late Neoproterozoic Baltic paleosol: intense weathering at high latitude? Geology 42, 323–326.
Liu, P., Liu, Y., Hu, Y., Yang, J., Pisarevsky, S.A., 2019. Warm climate in the "boring billion" era. Acta Geol. Sinica English Ed. 1 (93), 40–43.
Lyons, T.W., Reinhard, C.T., Planavsky, N.J., 2014. The rise of oxygen in Earth's early ocean and atmosphere. Nature 506, 307–315.
Mader, D., 1985. Fluvial conglomerates in continental red beds of the Buntsandstein (Lower Triassic) in the Eifel (FRG) and their palaeoenvironmental, palaeogeographical and palaeotectonic significance. Sed. Geol. 44, 1–64.
Markewich, H.W., Pavich, M.J., Buell, G.R., 1990. Contrasting soils and landscapes of the Piedmont and Coastal Plain, eastern United States. Geomorphology 3, 417–447.
Matsumoto, E., Naruoka, T., da Silva, E.F., 1997. Concentration of carbon dioxide in regolith air in different tropical geoecosystems of northeast Brazil. Inst. Geosci. Univ. Tsukuba Ann. Rept. 23, 11–15.
McBride, E.F., 1974. Significance of color in red, green, purple, olive, brown, and gray beds of Difunta Group, northeastern Mexico. J. Sediment. Res. 44, 760–773.
McFadden, L.D., McDonald, E.V., Wells, S.G., Anderson, K., Quade, J., Forman, S.L., 1998. The vesicular layer and carbonate collars of desert soils and pavements: formation, age and relation to climate change. Geomorphology 24, 101–145.
McMahon, S., van Smeerdijk Hood, A., McIlroy, D., 2017. The origin and occurrence of subaqueous sedimentary cracks. In: Brasier, A.T., McIlroy, D., McLoughlin, N. (Eds.), Earth System Evolution and Early Life: A Celebration of the Work of Martin Brasier. Geol. Soc. London Spec. Publ., pp. 285–309.
Meng, F., Zhou, C., Yin, L., Chen, Z., Yuan, X., 2005. The oldest known dinoflagellates: Morphological and molecular evidence from Mesoproterozoic rocks at Yongji, Shanxi Province. Chinese Sci. Bull. 50 (12), 1230–1234.
Meng, Y., Zuo, P., Zheng, D., Sun, F., Wang, P., Wang, Z., Li, Y., 2018. The earliest clastic sediments overlying the Xiong'er volcanic rocks: Implications for the Mesoproterozoic tectonics of the southern North China Craton. Precambr. Res. 305, 268–282.
Merkel, A., 2020. Climate data for cities worldwide. Website <https://en.climate-data.org>. (accessed August 26, 2020).
Mikucki, J.A., Pearson, A., Johnston, D.T., Turchyn, A.V., Farquhar, J., Schrag, D.P., Anbar, A.D., Priscu, J.C., Lee, P.A., 2009. A contemporary microbially maintained subglacial ferrous "ocean". Science 324, 397–400.
Mills, D.B., Ward, L.M., Jones, C., Sweeten, B., Forth, M., Treusch, A.H., Canfield, D.E., 2014. Oxygen requirements of the earliest animals. Proc. Nat. Acad. Sci. 111, 4168–4172.
Mitchell, R.L., Sheldon, N.D., 2010. The~ 1100 Ma Sturgeon Falls paleosol revisited: Implications for Mesoproterozoic weathering environments and atmospheric CO_2 levels. Precambr. Res. 183, 738–748.
Mukherjee, I., Large, R.R., Corkrey, R., Danyushevsky, L.V., 2018. The boring billion, a slingshot for complex life on Earth. Sci. Rep. 8 (1), 1–7.
Mukhopadhyay, J., Crowley, Q.G., Ghosh, S., Ghosh, G., Chakrabarti, K., Misra, B., Heron, K., Bose, S., 2014. Oxygenation of the Archean atmosphere: New paleosol constraints from eastern India. Geology 42, 923–926.
Murphy, C.P., 1983. Point counting pores and illuvial clay in thin section. Geoderma 31, 133–150.
Navarro-González, R., Rainey, F.A., Molina, P., Bagaley, D.R., Hollen, B.J., de la Rosa, J., Small, A.M., Quinn, R.C., Grunthaner, F.J., Cáceres, L., Gomez-Silva, B., 2003. Mars-like soils in the Atacama Desert, Chile, and the dry limit of microbial life. Science 302, 1018–1021.
Neaman, A., Chorover, J., Brantley, S.L., 2005a. Element mobility patterns record organic ligands in soils on early Earth. Geology 33, 117–120.
Neaman, A., Chorover, J., Brantley, S.L., 2005b. Implications of the evolution of organic acid moieties for basalt weathering over geological time. Am. J. Sci. 305, 147–185.
Nesbitt, H., Young, G.M., 1982. Early Proterozoic climates and plate motions inferred from major element chemistry of lutites. Nature 299, 715–717.
Noffke, N., 2010. In: Geobiology: Microbial Mats in Sandy Deposits from the Archean Era to Today. Springer, Berlin, p. 194.
Novoselov, A.A., de Souza Filho, C.R., 2015. Potassium metasomatism of Precambrian paleosols. Precambr. Res. 262, 67–83.
Ogg, J.G., Ogg, G.M., Gradstein, F.M., 2016. In: A Concise Geologic Time Scale: 2016. Elsevier, Amsterdam, p. 234.
Ohmoto, H., Watanabe, Y., Lasaga, A.C., Naraoka, H., Johnson, I., Brainard, J., Chorney, A., 2014. Oxygen, iron and sulfur geochemical cycles on the early Earth: problems and contradictions. In: Shaw, G.H. (Ed.), Earth's Early Atmosphere and Surface Environment. Geol. Soc. Amer. Spec. Pap., pp. 55–95.
Óskarsson, B.V., Riishuus, M.S., Arnalds, Ó., 2012. Climate-dependent chemical weathering of volcanic soils in Iceland. Geoderma 189, 635–651.
Pal, D.K., Wani, S.P., Sahrawat, K.L., Srivastava, P., 2014. Red ferruginous soils of tropical Indian environments: a review of the pedogenic processes and its implications for edaphology. Catena 121, 260–278.
Palmer, F.E., Staley, J.T., Murray, R.G.E., Counsell, T., Adams, J.B., 1986. Identification of manganese-oxidizing bacteria from desert varnish. Geomicrobiol J. 4, 343–360.
Pang, K., Tang, Q., Yuan, X.L., Wan, B., Xiao, S., 2015. A biomechanical analysis of the early eukaryotic fossil Valeria and new occurrence of organic-walled microfossils from the Paleo-Mesoproterozoic Ruyang Group. Palaeoworld 24, 251–262.
Paw, K.T.U., Xu, L., Ideris, A.J., Kochendorfer, J., Wharton, S., Rolston, D.E., Hsiao, T.C., 2006, Simultaneous carbon dioxide and oxygen measurements to improve soil efflux estimates. Kearney Foundation Soil Sci. Final Rept. 2004211, pp. 1−8.
Peacock, A.J., 1998. Oxygen at high altitude. Br. Med. J. 317, 1063–1066.
Peng, P., 2015. Late Paleoproterozoic-Neoproterozoic (1800–541 Ma) Mafic Dyke Swarms and Rifts in North China. In: Zhai, M.G. (Ed.), Precambrian Geology of China. Springer, Berlin, pp. 171–204.
Planavsky, N.J., Reinhard, C.T., Wang, X., Thomson, D., McGoldrick, P., Rainbird, R.H., Johnson, T., Fischer, W.W., Lyons, T.W., 2014. Low Mid-Proterozoic atmospheric oxygen levels and the delayed rise of animals. Science 346, 635–638.
Poulton, S.W., Canfield, D.E., 2011. Ferruginous conditions: a dominant feature of the ocean through Earth's history. Elements 7, 107–112.
Prave, A.R., 2002. Life on land in the Proterozoic: evidence from the Torridonian rocks of northwest Scotland. Geology 30, 811–814.
Pye, K., Sherwin, D., 1999. Loess. In: Goudie, A.S., Livingstone, I., Stokes, S. (Eds.), Aeolian Environments, Sediments and Landforms. Wiley, Chichester, pp. 213–238.
Raffi, R., Stenni, B., 2011. Isotopic composition and thermal regime of ice wedges in Northern Victoria Land, East Antarctica. Permafrost Periglac. Process. 22, 65 83.
Renaut, R.W., Tiercerlin, J.-J., 1994. Lake Bogoria, Kenya Rift Valley – a sedimentological overview. In: Renaut, R.W., Last, W.M. (Eds.), Sedimentology and Geochemistry of Modern and Ancient Saline Lakes. Soc. Sediment. Geol. Spec. Publ., pp. 101–124.
Retallack, G.J., 1977. Triassic palaeosols in the upper Narrabeen Group of New South Wales. Part I: Features of the palaeosols. J. Geol. Soc. Austral. 23, 383–399.
Retallack, G.J., 1983. Middle Triassic estuarine deposits near Benmore Dam, southern Canterbury and northern Otago, New Zealand. J. Roy. Soc. New Zealand 13, 107–127.
Retallack, G.J., 1991a. Untangling the effects of burial alteration and ancient soil formation. Ann. Rev. Earth Planet. Sci. 19, 183–206.
Retallack, G.J., 1991b. In: Miocene paleosols and ape habitats of Pakistan and Kenya. Oxford Univ. Press, New York, p. 346.
Retallack, G.J., 2005. Pedogenic carbonate proxies for amount and seasonality of precipitation in paleosols. Geology 33, 333–336.
Retallack, G.J., 2008. Cambrian palaeosols and landscapes of South Australia. Aust. J. Earth Sci. 55, 1083–1106.
Retallack, G.J., 2012a. Criteria for distinguishing microbial mats and earths. In: Noffke, N., Chafetz, H. (Eds.), Microbial mats in siliciclastic sediments. Soc. Econ. Paleont. Mineral. Spec. Pap., pp. 136–152.
Retallack, G.J., 2012b. Were Ediacaran siliciclastics of South Australia coastal or deep marine? Sedimentology 59, 1208–1236.
Retallack, G.J., 2013. Ediacaran life on land. Nature 493, 89–92.
Retallack, G.J., 2015a. Silurian vegetation stature and density inferred from fossil soils and plants in Pennsylvania, U.S.A. J. Geol. Soc. London 172, 693–709.
Retallack, G.J., 2015b. Acritarch evidence for an Ediacaran adaptive radiation of Fungi. Bot. Pacifica 4, 19–33.
Retallack, G.J., 2015c. Late Ordovician glaciation initiated by early land plant evolution and punctuated by greenhouse mass extinctions. J. Geol. 123, 509–538.
Retallack, G.J., 2016. Field and laboratory tests for recognition of Ediacaran paleosols. Gondwana Res. 36, 94–110.

Retallack, G.J., 2018. The oldest known paleosol profiles on Earth: 3.46 Ga Panorama Formation, Western Australia. Palaeogeogr. Palaeoclim. Palaeoec. 489, 230–248.
Retallack, G.J., 2019a. Interflag sandstone laminae, a novel sedimentary structure, with implications for Ediacaran paleoenvironments. Sed. Geol. 379, 60–76.
Retallack, G.J., 2019b. In: Soils of the Past. Wiley, Chichester, p. 534.
Retallack, G.J., 2020. Zebra rock and other Ediacaran paleosols in Western Australia. Aust. J. Earth Sci. https://doi.org/10.1080/08120099.2020.1820574.
Retallack, G.J., Broz, A.P., 2020. *Arumberia* and other Ediacaran-Cambrian fossils of central Australia. Hist. Biol. https://doi.org/10.1080/08912963.2020.175581.
Retallack, G.J., Huang, C.-M., 2010. Depth to gypsic horizon as a proxy for paleoprecipitation in paleosols of sedimentary environments. Geology 38, 403–406.
Retallack, G.J., Jahren, A.H., 2008. Methane release from igneous intrusion of coal during Late Permian extinction events. J. Geol. 116, 1–20.
Retallack, G.J., Mao, X., 2019. Paleoproterozoic (ca. 1.9 Ga) megascopic life on land in Western Australia. Palaeogeogr. Palaeoclim. Palaeoec. 532, 109266.
Retallack, G.J., Mindszenty, A., 1994. Well preserved Late Precambrian paleosols from northwest Scotland. J. Sedim. Res. A64, 264–281.
Retallack, G.J., Noffke, N., 2019. Are there ancient soils in the 3.7 Ga Isua Greenstone Belt, Greenland? Palaeogeogr. Palaeoclim. Palaeoec. 514, 18–30.
Retallack, G.J., Roering, J.J., 2012. Wave-cut or water-table platforms of rocky coasts and rivers. GSA Today 22 (6), 4–10.
Retallack, G.J., Krull, E.S., Thackray, G.D., Parkinson, D., 2013. Problematic urn-shaped fossils from a Paleoproterozoic (2.2 Ga) paleosol in South Africa. Precambr. Res. 235, 71–87.
Retallack, G.J., Krinsley, D.H., Fischer, R., Razink, J.J., Langworthy, K.A., 2016. Archean coastal-plain paleosols and life on land. Gondwana Res. 40, 1–20.
Rye, R., Holland, H.D., 1998. Paleosols and the evolution of atmospheric oxygen: a critical review. Am. J. Sci. 298, 621–672.
Serdyuchenko, D.P., 1968. Metamorphosed weathering crusts of the Precambrian: their metallogenis and petrographic fabric. In: Hetjman, B. (Ed.), Precambrian Geology. Proceedings 13th International Geological Congress Prague 4, pp. 37–42.
Sheldon, N.D., 2006. Precambrian paleosols and atmospheric CO_2 levels. Precambr. Res. 147, 148–155.
Sheldon, N.D., Retallack, G.J., 2001. Equation for compaction of paleosols due to burial. Geology 29, 247–250.
Sheldon, N.D., Tabor, N.J., 2013. Using paleosols to understand paleo-carbon burial. In: Dreise, S.G., Nordt, L. (Eds.), New Frontiers in Paleopedology and Terrestrial Paleoclimatology: Paleosols and Soil Surface Analog Systems. Soc Econ, Paleont. Mineral Spec. Publ., pp. 71–78.
Sheldon, N.D., Retallack, G.J., Tanaka, S., 2002. Geochemical climofunctions from North American soils and application to paleosols across the Eocene-Oligocene boundary in Oregon. J. Geol. 110, 687–696.
Sheldon, N.D., Mitchell, R.L., Dzombak, R.M., 2021. Reconstructing Precambrian pCO_2 and pO_2 using paleosols. In: Elements in Geochemical Tracers in Earth System Science, pp. 1–28. https://doi.org/10.1017/9781108870962.
Sohn, Y.K., Rhee, C.W., Kim, B.C., 1999. Debris flow and hyperconcentrated flood-flow deposits in an alluvial fan, northwestern part of the Cretaceous Yongdong Basin, Central Korea. J. Geol. 107 (1), 111–132.
Soil Survey Staff, 2014. In: Keys to Soil Taxonomy. Natural Resources Conservation Service, Washington DC, p. 358.
Som, S.M., Catling, D.C., Harnmeijer, J.P., Polivka, P.M., Buick, R., 2012. Air density 2.7 billion years ago limited to less than twice modern levels by fossil raindrop imprints. Nature 484, 359–362.
Som, S.M., Buick, R., Hagadorn, J.W., Blake, T.S., Perreault, J.M., Harnmeijer, J.P., Catling, D.C., 2016. Earth's air pressure 2.7 billion years ago constrained to less than half of modern levels. Nat. Geosci. 9, 448–451.
Stace, H.C.T., Hubble, G.D., Brewer, R., Northcote, K.H., Sleeman, J.R., Mulcahy, M.J., Hallsworth, E.G., 1968. In: A Handbook of Australian Soils. Rellim, Adelaide, p. 435.
Su, W., Li, H., Xu, L., Jia, S.H., Geng, J.Z., Zhou, H.Y., Wang, Z.H., Pu, H.Y., 2012. Luoyu and Ruyang Group at the south margin of the North China Craton (NCC) should belong in the Mesoproterozoic Changchengian System: Direct constraints from the LA-MC-ICPMS U-Pb age of the tuffite in the Luoyukou Formation, Ruzhou, Henan, China. Geol. Surv. Res. 35, 96–108.
Swineford, A., Frye, J.C., 1951. Petrography of the Peoria loess in Kansas. J. Geol. 59, 306–322.
Tang, D.-J., Shi, X.-Y., Jiang, G.-Q., Wang, X.-Q., 2011. Morphological association of microbially induced sedimentary structures (MISS) as a paleoenvironmental indicator: an example from the Proterozoic succession of the southern North China Platform. In: Noffke, N., Chafetz, H.S. (Eds.), Microbial Mats in Siliciclastic Depositional Systems through Time, Society for Sedimentary Geology. Society for Sedimentary Geology, Tulsa, Oklahoma, pp. 3–14.
Taylor-George, S., Palmer, F., Staley, J.T., Borns, D.J., Curtiss, B., Adams, J.B., 1983. Fungi and bacteria involved in desert varnish formation. Microbial Ecol. 9, 227–245.
Terry, R.D., Chilingar, G.V., 1955. Summary of "Concerning some additional aids in studying sedimentary formations," by MS Shvetsov. J. Sedim. Res. 25, 229–234.
Van Vliet-Lanoë, B., 1998. Frost and soils: implications for paleosols, paleoclimates and stratigraphy. Catena 34, 157–183.
Vepraskas, M.J., Sprecher, S.W., 1997. Summary. In: Vepraskas, M.J., Sprecher, S.W. (Eds.), Aquic Conditions and Hydric Soils: The Problem Soils. Soil Sci. Soc. Amer. Spec, Publ.,, pp. 153–156.
Voigt, C., Klipsch, S., Herwartz, D., Chong, G., Staubwasser, M., 2020. The spatial distribution of soluble salts in the surface soil of the Atacama Desert and their relationship to hyperaridity. Global Planet. Change 184, 103077.
Wallace, M.W., Hood, A.S., 2018. Zebra textures in carbonate rocks: Fractures produced by the force of crystallization during mineral replacement. Sed. Geol. 368, 58–67.
Watson, A., 1985. Structure, chemistry and origins of gypsum crusts in southern Tunisia and the central Namib Desert. Sedimentology 32, 855–875.
Weinberger, R., 2001. Evolution of polygonal patterns in stratified mud during desiccation: the role of flaw distribution and layer boundaries. Geol. Soc. Amer. Bull. 113, 20–31.
Wittkop, C., Swanner, E.D., Grengs, A., Lambrecht, N., Fakhraee, M., Myrbo, A., Bray, A. W., Poulton, S.W., Katsev, S., 2020. Evaluating a primary carbonate pathway for manganese enrichments in reducing environments. Earth Planet. Sci. Lett. 538, 116201.
Wordsworth, R., Pierrehumbert, R., 2013. Hydrogen-nitrogen greenhouse warming in Earth's early atmosphere. Science 339, 64–67.
Wu, S.P., Chen, Z.S., 2005. Characteristics and genesis of Inceptisols with placic horizons in the subalpine forest soils of Taiwan. Geoderma 125, 331–341.
Yang, S.P., Zhou, H.R., 1995. Trace fossils from the Precambrian Ruyang Group of western Henan. Geol. Rev. 41, 205–210.
Yarnold, J.C., 1993. Rock-avalanche characteristics in dry climates and the effect of flow into lakes: insights from mid-Tertiary sedimentary breccias near Artillery Peak, Arizona. Geol. Soc. Am. Bull. 105, 345–360.
Yin, L.M., 1997. Acanthomorphic acritarchs from Meso-Neoproterozoic shales of the Ruyang Group, Shanxi, China. Rev. Palaeobot. Palynol. 98, 15–25.
Yin, L.-M., Bian, L., Yuan, X., 2004. Discovery of branched tubular algae and microscopic tubes with annular-helical thickening from the Mesoproterozoic Ruyang Group of Shanxi, North China. Sci. China D Earth Sci. 47, 880–885.
Yin, L.-M., Yuan, X.-L., Yuan, F.-W., Huang, J.-M., 2005. Protists of the Upper Mesoproterozoic Ruyang Group in Shanxi Province, China. Precambrian Res. 141, 49–66.
Yin, L.-M., Yuan, X.-L., 2007. Radiation of Meso-Neoproterozoic and early Cambrian protists inferred from the microfossil record of China. Palaeogeogr. Palaeoclim. Palaeoec. 254, 350–361.
Yue, L., Liu, Z., Ma, Y., 2018. Sedimentary environment and depositional evolution of the Mesoproterozoic Bingmagou Formation on the southern margin of the North China Craton. Sci. Rep. 8 (1), 1–12.
Zakrzewska, B., 1963. An analysis of landforms in a part of the central Great Plains. Ann. Assoc. Am. Geograph. 53, 536–568.
Zhang, S., Han, Y., Dong, J., Wu, H., Li, Z., Li, H., Bai, Z., 2009. Proterozoic paleogeographic positions of the North China Craton: new geochronological and paleomagnetic constraints. Amer. Geophys. Union Field Meet. 2009, GP21A-0756.
Zhang, S., Li, Z.X., Evans, D.A., Wu, H., Li, H., Dong, J., 2012. Pre-Rodinia supercontinent Nuna shaping up: a global synthesis with new paleomagnetic results from North China. Earth Planet. Sci. Lett. 353, 145–155.
Zhao, T.P., Zhou, M.F., Zhai, M., Xia, B., 2002. Paleoproterozoic rift-related volcanism of the Xiong'er Group, North China craton: implications for the breakup of Columbia. Int. Geol. Rev. 44 (4), 336–351.
Zhao, T., Zhai, M., Xia, B., Li, H., Zhang, Y., Wan, Y., 2004. Zircon U-Pb SHRIMP dating for the volcanic rocks of the Xiong'er Group: Constraints on the initial formation age of the cover of the North China Craton. Chin. Sci. Bull. 49 (23), 2495–2502.
Zheng, D.S., Zheng, W., Wang, J., Wu, L., Ren, Z.H., Su, Z.K., Meng, F.Q., Wang, Y.W., Yan, J.W., 2011. Characteristic of red sandstone and its environment significance in Yunmengshan Formation of Mesoproterozoic in Yuntai Mount. J. Henan Polytech. Univ. Nat. Sci. 30, 534–538.
Zheng, D.S., Wang, P.X., Sun, F.B., 2016. Sedimentary environment of Mesoproterozoic Bingmagou Formation in Yichuan, Western Henan Province. Geol. Sci. Technol. Inf. 35, 1–7.
Zheng, D.S., Meng, Y., Sun, F.B., Wang, P.X., 2017. REE geochemical characteristics of sandstones of Mesoproterozoic Bingmagou Formation in Yichuan. J. Henan Polytech. Univ. Nat. Sci. 36, 38–45.
Zheng, W., Sun, F.Y., 2011. Macro-analysis on the microbially induced sedimentary structures features and sedimentary environmental evolution in the Ruyang Group of Lushan, Western Henan. Geol. Surv. Res 34, 170–178.
Zheng, W., Qi, Y.-A., Liu, S.-X., Zhang, Z., 2008. Classification and genetic analysis of ripple marks on Yunmengshan Formation of Yuntaishan World Geopark, Henan province. J. Henan Polytech. Univ. Nat. Sci. 4, 399–403.
Zheng, W., Qi, Y.A., Xing, Z.F., Yuan, Y.Y., 2012. Microbially induced sedimentary structures and sedimentary environments of the Ruyang Group in Lushan, western Henan. Sediment. Geol. Tethyan Geol. 1, 1–4.
Ziegenbalg, S.B., Brunner, B., Rouchy, J.M., Birgel, D., Pierre, C., Böttcher, M.E., Caruso, A., Immenhauser, A., Peckmann, J., 2010. Formation of secondary carbonates and native sulphur in sulphate-rich Messinian strata, Sicily. Sediment. Geology 227, 37–50.
Zillen, L.M., Snowball, I.F., Sandgren, P., Stanton, T., 2003. Occurrence of varved lake sediment sequences in Vamtland, west central Sweden: lake characteristics, varve chronology and AMS radiocarbon dating. Boreas 32, 612–626.
Zuo, P., Li, Y., Zhang, G., Si, R., Wang, S., Liu, S., Zheng, D., Sun, J., 2019. Reviews of the Mesoproterozoic to Neoproterozoic sedimentary sequences and new constraints on the tectono-sedimentary evolution of the southern margin of the North China Craton. J. Asian Earth Sci. 179, 416–429.